

The linear response function of an idealized atmosphere: construction using Green's functions, applications, and implications for the practical use of the fluctuation-dissipation theorem

PEDRAM HASSANZADEH*

Department of Earth and Planetary Sciences and Center for the Environment, Harvard University, Cambridge, Massachusetts

ZHIMING KUANG

Department of Earth and Planetary Sciences and John A. Paulson School of Engineering and Applied Sciences, Harvard University, Cambridge, Massachusetts

ABSTRACT

A linear response function (LRF) determines the mean-response of a nonlinear climate system to weak imposed forcings, and an eddy flux matrix (EFM) determines the eddy momentum and heat flux responses to mean-flow changes. Neither LRF nor EFM can be calculated from first principles due the lack of a complete theory for turbulent eddies. Here the LRF and EFM for an idealized dry atmosphere are computed by applying numerous localized weak forcings, one at a time, to a GCM with Held-Suarez physics and calculating the mean-responses. The LRF and EFM for zonally-averaged responses are then constructed using these forcings and responses through matrix inversion. Tests demonstrate that LRF and EFM are fairly accurate. Spectral analysis of the LRF shows that the most excitable dynamical mode, the neutral vector, strongly resembles the model's Annular Mode. The framework described here can be employed to compute the LRF/EFM for zonally-asymmetric responses and more complex GCMs. The potential applications of the LRF/EFM constructed here are i) forcing a specified mean-flow for hypothesis-testing, ii) isolating/quantifying the eddy-feedbacks in complex eddy-mean flow interaction problems, and iii) evaluating/improving more generally-applicable methods currently used to construct LRFs or diagnose eddy-feedbacks in comprehensive GCMs or observations. As an example for iii, the LRF is also computed using the fluctuation-dissipation theorem (FDT), and the previously-calculated LRF is exploited to investigate why FDT performs poorly in some cases. It is shown that dimension-reduction using leading EOFs, which is commonly used to construct LRFs from the FDT, can significantly degrade the accuracy due to the non-normality of the operator.

1. Introduction

How the different components of the climate system respond to imposed forcings is of significant importance for understanding the internal climate variability and anthropogenic climate change. For an external forcing \mathbf{f} that is weak enough so that the response of the nonlinear climate system varies linearly with \mathbf{f} , the problem can be formulated as (Palmer 1999)

$$\dot{\mathbf{x}} = \mathbf{L}\mathbf{x} + \mathbf{f} \quad (1)$$

where \mathbf{x} is the state-vector response, i.e., deviation from the time-mean flow (*mean-flow* hereafter) of the unforced ($\mathbf{f} = 0$) system, and \mathbf{L} is the linear response function (LRF) of the system (see section 2 for details). If \mathbf{L} is known, we can immediately calculate not only the responses to various scenarios of external forcings (which can also be ob-

tained from usually-expensive GCM simulations), but we can also find the forcing needed to achieve a prescribed response (the inverse problem), the most effective forcing (i.e., forcing producing the largest response), and the most excitable dynamical mode, i.e., the so-called *neutral vector*, which is important for both internal variability and forced response (Marshall and Molteni 1993; Goodman and Marshall 2002).

Another problem of great interest is how eddies respond to changes in the mean-flow (which here refers to the flow averaged over an appropriate timescale much longer than the eddy timescale). Focusing on synoptic eddies in the atmosphere, for instance, the increase of eddy phase-speed in response to strengthening of the lower stratospheric winds (Chen and Held 2007) and the increase of eddy length-scale in response to changes in the atmosphere's thermal structure (Kidston et al. 2011; Riviere 2011) have been suggested to cause the observed and projected poleward shift of the midlatitude jets. As another example, changes in the eddy momentum and heat fluxes in re-

*Corresponding author address: Pedram Hassanzadeh, 24 Oxford Street, Cambridge, MA 02138.
E-mail: hassanzadeh@fas.harvard.edu

sponse to changes in the tropospheric zonal-wind and temperature play a critical role in the dynamics of the leading pattern of variability in the midlatitudes, i.e., the Northern and Southern Annular Modes (Robinson 2000; Lorenz and Hartmann 2001), while the tropospheric eddy flux response to stratospheric changes are important for the tropospheric-stratospheric coupling (Haynes et al. 1991; Kushner and Polvani 2004; Song and Robinson 2004). The eddies modify the mean-flow through the eddy momentum and heat fluxes, which can be quantified, for example, using the Eliassen-Palm flux (Edmon et al. 1980). The mean-flow also modifies the eddies. What complicates the eddy-mean flow interaction problems, not only in the atmosphere but also in other turbulent geophysical flows (Vallis 2006, chs. 7-10), is that, despite extensive efforts, how eddy fluxes respond to a change in the mean-flow is not fully understood and a complete theory for this response is currently unavailable (Held 2000; Schneider 2006). For example, as described in section 2, for the zonal-mean response in an idealized dry atmosphere (which is the focus of this paper), the state-vector consists of \bar{u} and \bar{T} , and the problem can be formulated as

$$\begin{bmatrix} \langle \bar{u}'v' \rangle \\ \langle \bar{v}'T' \rangle \end{bmatrix} = \mathbf{E} \begin{bmatrix} \langle \bar{u} \rangle \\ \langle \bar{T} \rangle \end{bmatrix} \quad (2)$$

where the overbars and $\langle \cdot \rangle$ denote, respectively, the zonal-means and time-means; \bar{u} and \bar{T} are the responses in zonal-mean zonal-wind and temperature; and $\langle \bar{u}'v' \rangle$ and $\langle \bar{v}'T' \rangle$ are the responses of eddy momentum and heat fluxes to $\langle \bar{u} \rangle$ and $\langle \bar{T} \rangle$. In this paper we refer to \mathbf{E} as the eddy flux matrix (EFM), which with the current state of understanding cannot be determined from the first principles.

The two issues discussed above are related: a major difficulty in calculating the LRFs is to accurately account for the eddy-feedbacks (because \mathbf{E} is unknown), and as a result even in very simple models of the climate system, finding the LRFs remains a challenge. For example, in the Held-Suarez benchmark setup (Held and Suarez 1994), where the focus is on a dry atmosphere with simply zonally-symmetric boundary conditions and parametrization of radiation and planetary boundary-layer with, respectively, Newtonian cooling and Rayleigh drag, the LRF consists of four components: mean-flow advection, surface friction, Newtonian relaxation, and eddy-feedbacks. While in this setup the first three components are known analytically for a given mean-flow, the eddy-feedback is not, which renders the LRF indeterminable analytically.

The three common approaches to finding LRFs involve neglecting the eddy-feedbacks, parameterizing the eddy-feedbacks, or employing the fluctuation-dissipation theorem (FDT). The first approach is similar to the hydrodynamic stability analysis where the equations of motion are linearized around a mean-flow and all nonlinear terms (which contain eddy fluxes) are ignored (Vallis

2006, ch. 6). Such an approach has provided valuable insight into some aspects of the atmospheric circulation (Hoskins and Karoly 1981; Marshall and Molteni 1993; Goodman and Marshall 2002), but because of the lack of eddy-feedbacks, can result in inaccurate LRFs (e.g., Branstator and Haupt 1998) and LRFs with linearly unstable modes, which suggests, from Eq. (1), unbounded growth of \mathbf{x} . Accounting for the eddy-feedbacks using diffusive (e.g., Pavan and Held 1996; Lapeyre and Held 2003; Vallis 2006, ch. 10) or stochastic (e.g., Farrell and Ioannou 1996a,b, 2003; Zhang and Held 1999) closures might improve the accuracy of the LRF, but there are challenges associated with using these parameterizations in complex models, see, e.g., the reviews by Franzke et al. (2015), DelSole (2004) and Berner et al. (2015).

The FDT, a powerful tool in statistical physics (Nyquist 1928; Kubo 1966), suggest that the LRF can be built for a GCM from lag-covariances of a long unforced simulation and even for the climate system itself from observations (Leith 1975). In principle, the FDT can produce a LRF that accurately takes into account the eddy-feedbacks and any other physical process that is present in the model or nature without the need for a detailed understanding of these processes. However, there are uncertainties in applicability of the FDT to the climate system, and testing FDT in GCMs (e.g., Gritsun and Branstator 2007; Ring and Plumb 2008; Fuchs et al. 2015) and simple models of geophysical turbulence (e.g., Majda et al. 2010; Lutsko et al. 2015) have produced mixed results. The FDT is further discussed in section 7.

In this paper we take a different approach to finding the LRF (with accurate eddy-feedbacks) and EFM of a relatively simple GCM. We use Green's functions following the framework developed in Kuang (2010) to calculate the LRF for a cloud-system-resolving model, which has been used to study convectively-coupled waves (Kuang 2010), Walker cells (Kuang 2012), and convective parameterization schemes (Nie and Kuang 2012; Herman and Kuang 2013). With problems in large-scale atmospheric circulation in mind, here we focus on the zonally-averaged forcings and responses of an idealized dry GCM, where the state-vector consists only of \bar{u} and \bar{T} (see section 2 for details). The procedure to find the LRF and EFM is explained in details in section 3; briefly, weak spatially-confined forcings of zonal-wind and temperature are applied in the dry dynamical core with Held-Suarez physics at 100 latitude-pressure combinations one at a time. For each forcing, the time-mean response ($\langle \bar{u} \rangle$, $\langle \bar{T} \rangle$) is calculated from a long integration, and the responses and imposed forcings from all runs are then used to find the LRF from the long-time averaged Eq. (1) using matrix inversion. Similarly, $\langle \bar{u}'v' \rangle$ and $\langle \bar{v}'T' \rangle$ are calculated for all the runs and along with time-mean responses are used to find the EFM from Eq. (2) using matrix inversion.

The remainder of this paper is structured as follows. In section 2 we discuss Eqs. (1)-(2) and the underlying assumptions, followed by descriptions of the model setup and the detailed procedure for calculating the LRF and EFM in section 3. Several tests to validate the calculated LRF and EFM are presented in section 4 which show that the LRF is fairly skillful in finding the time-mean response to a given zonally-symmetric external forcings and vice versa, and that the EFM can quantify the time-mean response of eddy fluxes to a change in the mean-flow reasonably well. In section 5 we present some of the properties of the LRF of the idealized dry atmosphere. In particular, we show that the neutral vector (i.e., the most excitable dynamical mode) is fairly similar to the Annular Modes, which offers some insight into the reason behind the ubiquity of Annular Mode-like patterns in the response of the real and modeled atmospheres to forcings. Potential applications of the calculated LRF and EMF are discussed in section 6, which include i) forcing a specified mean-flow for hypothesis-testing in the idealized GCM, e.g., as used in Hassanzadeh and Kuang (2015) to probe causality in the relationship between the negative phase of Arctic Oscillation and increased blocking, ii) isolating and quantifying the eddy-feedbacks in complex eddy-mean flow interaction problems, and iii) examining and evaluating more generally-applicable methods that are currently employed to diagnose eddy-feedbacks or construct LRFs in more complex GCMs. As an example for iii, in section 7 we calculate, for the same idealized model, the LRF using the FDT and investigate the source(s) of its poor performance for some tests by employing the LRF calculated using the Green's function. We show that for non-normal operators, dimension-reduction by projecting the data onto the leading EOFs, which is commonly used to construct LRFs from the FDT, can significantly degrade the accuracy. Readers who are mainly interested in FDT might skip sections 3-6. The paper is summarized in section 8.

2. Formulation

We start with the derivation of Eq. (1) for zonally-averaged forcings/responses, which, although straightforward, helps with better understanding the underlying assumptions. The zonally-averaged equations of the climate system can be written as

$$\dot{\bar{\mathbf{X}}} = \mathbb{F}(\bar{\mathbf{X}}) \quad (3)$$

where the state-vector $\bar{\mathbf{X}}$ is a set of zonally-averaged variables that we assume can uniquely describe the system and \mathbb{F} is a nonlinear function that represents the relevant physical processes and describes the evolution of $\bar{\mathbf{X}}$. For the purpose of this paper, Eq. (3) is the zonally-averaged primitive equations with Held-Suarez physics (Held and Suarez

1994) with the additional assumption that eddies (defined as deviations from the zonal-mean) are in statistical-equilibrium with the state-vector $\bar{\mathbf{X}}$ so that the eddy fluxes can be uniquely determined from $\bar{\mathbf{X}}$. This assumption and the other assumptions related to the state-vector are further discussed later in this section.

If the system's state-vector evolves from $\bar{\mathbf{X}}(t)$ to $\langle \bar{\mathbf{X}} \rangle + \bar{\mathbf{x}}(t)$ in response to an external forcing $\bar{\mathbf{f}}(t)$ of zonal torque or buoyancy, where $\langle \bar{\mathbf{X}} \rangle$ is the mean-flow of the unforced state-vector $\bar{\mathbf{X}}$, Eq. (3) becomes

$$\dot{\bar{\mathbf{x}}} = \mathbb{F}(\langle \bar{\mathbf{X}} \rangle + \bar{\mathbf{x}}) + \bar{\mathbf{f}} \quad (4)$$

It should be clarified that in this section and the rest of the paper “mean-flow” and $\langle \cdot \rangle$ denote very long-term averages so that $\mathbb{F}(\langle \bar{\mathbf{X}} \rangle) = 0$. A Taylor expansion of \mathbb{F} around $\langle \bar{\mathbf{X}} \rangle$ yields Eq. (1) for the state-vector response $\bar{\mathbf{x}}$, which as mentioned earlier is a set of zonal-mean variables:

$$\dot{\bar{\mathbf{x}}} = \left. \frac{d\mathbb{F}}{d\bar{\mathbf{X}}} \right|_{\langle \bar{\mathbf{X}} \rangle} \bar{\mathbf{x}} + \bar{\mathbf{f}} = \mathbf{L} \bar{\mathbf{x}} + \bar{\mathbf{f}} \quad (5)$$

where we have assumed that the terms of order $\bar{\mathbf{x}}^2$ and higher are negligible compared to the term that is linear in $\bar{\mathbf{x}}$ (assumption 1). The LRF \mathbf{L} is thus the Jacobian of $\mathbb{F}(\bar{\mathbf{X}})$ evaluated at $\langle \bar{\mathbf{X}} \rangle$. See Palmer (1999) and Farrell and Ioannou (1996a,b) for further discussions of the above equations from a dynamical-system perspective.

It should be noted that ignoring terms that are nonlinear in $\bar{\mathbf{x}}$ does not eliminate the eddy-feedbacks from \mathbf{L} in Eq. (5), and the difference between this equation and the equation that could be derived following the first approach discussed in section 1 (i.e., linearization of the equations of motion) should be emphasized: the eddy fluxes are absent in the latter while they are linearized and represented as a function of $\bar{\mathbf{x}}$ in (5). For such representation to be valid, we have to assume that synoptic eddies respond instantaneously to changes in $\bar{\mathbf{x}}$, or said another way, the eddy statistics are always in quasi-equilibrium with $\bar{\mathbf{x}}$ (assumption 2). This is justified if $\bar{\mathbf{x}}$ has timescales of a few days or longer; to satisfy this requirement, we assume that $\bar{\mathbf{x}}$ is anomaly averaged over several days, which is appropriate for zonal-means in many large-scale phenomena of interest.

We also note the difference between our approach to finding the LRF in Eq. (5) and the second approach discussed in section 1, where the eddy fluxes are parametrized (as done here) but the relationship between the eddy fluxes and the mean-flow is assumed to be known from a turbulent closure approximation. Here we calculate the LRF from a fully nonlinear eddy-resolving model instead of making such assumption about this relationship.

It should be further clarified that the external forcing $\bar{\mathbf{f}}$ refers to any mechanical or thermal forcing exerted by unresolved or unrepresented processes and phenomena,

including climate change-induced forcings such as high-latitude warming (i.e., Arctic Amplification), tropical tropospheric warming (due to latent heating), and stratospheric cooling (due to ozone depletion) (Butler et al. 2010). In light of the above assumption on the timescale of $\bar{\mathbf{x}}$, external forcing \mathbf{f} may also represent the stochastic eddy forcing generated by the atmospheric internal dynamics at (unresolved) short timescales and small spatial-scales.

The next question to answer is what variables constitute $\bar{\mathbf{x}}$. The state-vector \mathbf{X} of the primitive equations of the Held-Suarez setup involve five variables: zonal U , meridional V , and vertical Ω velocities, temperature Θ , and geopotential height Φ (in practice, the numerical algorithm of the dry dynamical core is designed to solve for vertical vorticity, horizontal divergence, temperature, and surface pressure). Although the zonal-mean responses of these five variables ($\bar{u}, \bar{v}, \bar{\omega}, \bar{T}, \bar{\phi}$) can be used for $\bar{\mathbf{x}}$, it is desirable to reduce the number of variables to lower the computational cost of finding the LRF and EFM. To reduce $\bar{\mathbf{x}}$, first we highlight that the zonally-averaged mean-flow of the response consists of \bar{u} and \bar{T} , which are closely in gradient-wind balance except near the equator, and \bar{v} and $\bar{\omega}$, which form the meridional circulation and can be represented by a single streamfunction χ via the continuity equation. We can choose

$$\bar{\mathbf{y}} = \begin{bmatrix} \bar{u} \\ \bar{T} \end{bmatrix} \quad (6)$$

if we further assume that \bar{u} and \bar{T} are in gradient-wind balance, which is very reasonable outside the deep tropics (assumption 3).

As outlined in Appendix A, with assumptions 2 and 3, χ can be determined for a given $(\bar{u}, \bar{T}, \bar{f})$ from a diagnostic equation, and the system can be completely defined by (\bar{u}, \bar{T}) . As a result, the state-vector reduces to (6), and Eq. (5) reduces to

$$\dot{\bar{\mathbf{y}}} = \mathbf{M}\bar{\mathbf{y}} + \bar{\mathbf{f}}_{\text{eff}}. \quad (7)$$

where the size and elements of \mathbf{M} , the LRF of the reduced system (7), are different from \mathbf{L} , but they contain the same physics: Rayleigh drag, Newtonian cooling, eddy-feedback, meridional advection of (\bar{u}, \bar{T}) by $(\langle \bar{v} \rangle, \langle \bar{\Omega} \rangle)$, and meridional advection of $(\langle \bar{U} \rangle, \langle \bar{\Theta} \rangle)$ by χ . The effective external forcing $\bar{\mathbf{f}}_{\text{eff}} = \mathbf{B}\mathbf{f}$ has size, elements, and physics that are different from \mathbf{f} : the latter is the direct external forcing in $(\bar{U}, \bar{\Theta})$ that is applied to the atmosphere, while the effective forcing includes this direct forcing plus changes in χ due to the component of \mathbf{f} that is not in gradient-wind balance. This is related to the classic Eliassen balanced flow problem (Eliassen 1951) and is further discussed in Appendix A. We are mainly interested in finding

$$\tilde{\mathbf{M}} = \mathbf{B}^{-1}\mathbf{M} \quad (8)$$

which relates time-mean response $\langle \bar{\mathbf{y}} \rangle$ to the direct external forcing $\langle \mathbf{f} \rangle$ as

$$\tilde{\mathbf{M}}\langle \bar{\mathbf{y}} \rangle = -\langle \mathbf{f} \rangle \quad (9)$$

In summary, Eqs. (6)-(9) require the following assumptions

1. The forcing is weak enough so that the system is in the linear regime (i.e., $\bar{\mathbf{y}}$ depends linearly on \mathbf{f}).
2. Eddies respond instantaneously to changes in \bar{u} and \bar{T} , which is justified for phenomena with timescales of a few days and longer.
3. \bar{u} and \bar{T} are in gradient-wind balance, which is very reasonable outside the deep tropics.

Note that with further assumptions, including insensitivity of eddy fluxes to changes in mean static stability, the state-vector could be reduced to only one variable (e.g., \bar{u}) as described in Ring and Plumb (2008, section 5). Here we use (6).

3. Construction of the LRF and EFM

a. Idealized Dry GCM

We use the GFDL dry dynamical core, which is a pseudo-spectral GCM that solves the primitive equations on sigma levels σ . The model is used with the Held-Suarez setup, which is described in details in Held and Suarez (1994). Briefly, the model is forced by Newtonian relaxation of temperature to a prescribed equinoctial radiative-equilibrium state with a specified equator-to-pole surface temperature difference of 60 K. The relaxation timescale is 40 days except at the lower-level tropics where it is changed to 4 days to create a more realistic Hadley circulation. Rayleigh drag with a prescribed rate, which decreases linearly from 1 day^{-1} at the surface ($\sigma = 1$) to zero at $\sigma = 0.7$ and higher levels, is used to remove momentum from the low-levels, and ∇^8 hyperdiffusion is used to remove enstrophy at small scales. The forcings, dissipations, and boundary conditions are all zonally-symmetric and symmetric between the two hemispheres. A T63 spectral resolution ($\sim 1.9^\circ \times 1.9^\circ$) with 40 equally-spaced sigma levels and 15 min time-steps are used to solve the equations. Unless noted otherwise, every run is 45000 days with the last 44500 days used to calculate time-means denoted with $\langle \cdot \rangle$. “Ensemble” refers to three runs with identical setup and slightly different initial conditions.

b. Procedure

Instead of forcing the model at every pressure p (40 levels) and latitude μ (96 grid points), we use a set of 100

basis functions with coarser resolution to reduce the computational cost. The basis functions are of the Gaussian form

$$\exp \left[-\frac{(|\mu| - \mu_o)^2}{\mu_w^2} - \frac{(p - p_o)^2}{p_w^2} \right] \quad (10)$$

where $\mu_w = 10^\circ$, $\mu_o = 0^\circ, 10^\circ, 20^\circ, \dots, 90^\circ$, $p_w = 75$ hPa, and $p_o = 100, 200, 300, \dots, 1000$ hPa (p is the full-level pressure in the model). Zonally-symmetric time-invariant forcings of U or Θ are added at each basis function one at a time. To be clear, this forcing is added to the right-hand side of the zonal-momentum or temperature equation in the GCM and is therefore the direct external forcing $\bar{\mathbf{f}}$ (not the effective forcing). Each of these forced runs are referred to as a “trial” hereafter. Note that the forcings are added to both hemispheres simultaneously. The amplitude of forcing \bar{f}_o in each trial is chosen to obtain a large signal-to-noise ratio within the linear regime (see Appendix B for details). Each trial is used to calculate $\langle \bar{U} \rangle$ and $\langle \bar{\Theta} \rangle$ interpolated on 39 pressure levels (25, 50, 75, \dots , 975 hPa). For each variable (U or Θ), two trials with $\pm \bar{f}_o$ are run for each (μ_o, p_o) and the results are combined as $\langle \bar{u} \rangle = (\langle \bar{U} \rangle_+ - \langle \bar{U} \rangle_-)/2$ and $\langle \bar{T} \rangle = (\langle \bar{\Theta} \rangle_+ - \langle \bar{\Theta} \rangle_-)/2$ where the subscript $+$ ($-$) denotes the trial with $+\bar{f}_o$ ($-\bar{f}_o$). Combining the results cancels the quadratic terms in the Taylor expansion of Eq. (4) and improves the accuracy of Eq. (5). A total of 400 trials are needed to calculate the LRF and EMF. An ensemble of unforced simulations (referred to as the control-run and denoted with subscript c) is run as well.

Once the 400 acceptable trials are chosen following the quantitative and qualitative criteria described in Appendix B, the hemispherically-averaged results of the trials with positive and negative forcings are combined to obtain 200 sets of $(\langle \bar{u} \rangle, \langle \bar{T} \rangle)$. The $(\langle \bar{u} \rangle, \langle \bar{T} \rangle)$ of each set are then projected onto the 100 basis functions (10) using least-square linear regression. This results in $\langle \bar{\mathbf{u}} \rangle_n$ and $\langle \bar{\mathbf{T}} \rangle_n$ which are column vectors of length 100 containing the regression coefficients of the response to forcing $\bar{\mathbf{f}}_n$ ($n = 1, 2, \dots, 200$). $\bar{\mathbf{f}}_n$ is a column vector of length 100 whose elements are all zero except for its n th element which is the forcing amplitude of the n th basis function (forcing for $n = 1 - 100$ is imposed torque and for $n = 101 - 200$ is thermal forcing). We then assemble the response matrix \mathbf{R} (11) and the forcing matrix \mathbf{F} (12), which are 200×200 matrices:

$$\mathbf{R} = \begin{bmatrix} \langle \bar{\mathbf{u}} \rangle_1 & \langle \bar{\mathbf{u}} \rangle_2 & \dots & \langle \bar{\mathbf{u}} \rangle_{101} & \dots & \langle \bar{\mathbf{u}} \rangle_{200} \\ \langle \bar{\mathbf{T}} \rangle_1 & \langle \bar{\mathbf{T}} \rangle_2 & \dots & \langle \bar{\mathbf{T}} \rangle_{101} & \dots & \langle \bar{\mathbf{T}} \rangle_{200} \end{bmatrix} \quad (11)$$

$$\mathbf{F} = \begin{bmatrix} \bar{\mathbf{f}}_1 & \bar{\mathbf{f}}_2 & \dots & \mathbf{0} & \dots & \mathbf{0} \\ \mathbf{0} & \mathbf{0} & \dots & \bar{\mathbf{f}}_{101} & \dots & \bar{\mathbf{f}}_{200} \end{bmatrix} \quad (12)$$

where $\mathbf{0}$ is a 200×1 zero matrix, and \mathbf{F} is a diagonal matrix. Equation 9 is then used to calculate $\tilde{\mathbf{M}}$:

$$\tilde{\mathbf{M}} = -\mathbf{F}\mathbf{R}^{-1}. \quad (13)$$

As discussed in Kuang (2010), because (13) involves \mathbf{R}^{-1} , the eigenvalues of $\tilde{\mathbf{M}}$ (denoted as λ) have uncertainties ($\delta\lambda$) that scale as $|\delta\lambda| \propto \lambda^2 \|\delta\mathbf{R}\|$, where $\|\cdot\|$ is a matrix norm and $\delta\mathbf{R}$ is the errors in \mathbf{R} (note that \mathbf{F} is imposed and hence precisely known). As a result, the errors in \mathbf{R} have the least (most) influence on the eigenvalues of $\tilde{\mathbf{M}}$ with the smallest (largest) magnitude, which are calculated with the highest (lowest) accuracy. In fact, recalculating $\tilde{\mathbf{M}}$ using several of the trials replaced with runs with slightly different \bar{f}_o results in substantial changes in the modes with large $|\lambda|$, while the modes with small $|\lambda|$ are robust. It is a desired property that the slowest decaying modes (with timescales of a few days and longer) are accurately calculated, because these are the modes relevant to the large-scale circulation (e.g., Annular Modes have timescales on the order of tens of days). Fast modes (timescale of 1 day or shorter), which are inaccurately calculated and also violate assumption 2, have timescales much shorter than that of the large-scale circulation. All but five of the eigenmodes of the computed $\tilde{\mathbf{M}}$ are decaying (λ has negative real part) where the slowest decaying mode has $\lambda \sim -0.017 \text{ day}^{-1}$. The eigenvalues of $\tilde{\mathbf{M}}$ with timescales longer than 1 day are shown in Fig. S1 (Supplemental Material) and the eigenvalues/vectors are further discussed in section 5. The five growing eigenmodes have λ with real and imaginary parts on the orders of $100 - 1000 \text{ day}^{-1}$, which is much faster than the shortest timescale resolved in the GCM (i.e., the 15 min timestep).

The five growing modes are evidently erroneous and following Kuang (2010), the sign of eigenvalues for these modes are reversed and the matrix is reconstructed using the eigenvectors/eigenvalues. Hereafter, $\tilde{\mathbf{M}}$ refers to this matrix, which only has decaying modes. The rapidly decaying modes with large $|\lambda|$ on the order of $10 - 1000 \text{ day}^{-1}$ are also inaccurate. These modes do not affect calculations that involve $\tilde{\mathbf{M}}^{-1}$ multiplication (such as calculating the response to a given forcing); however, they degrade the accuracy of calculations that involve $\tilde{\mathbf{M}}$ multiplication. For example, these modes can result in unphysically large forcings calculated for a given response. This problem is solved by filtering out the fast-decaying inaccurate modes by calculating matrix $\hat{\mathbf{M}}$ as

$$\hat{\mathbf{M}} = \frac{\exp[\tilde{\mathbf{M}}\varepsilon] - \mathbf{I}}{\varepsilon} \quad (14)$$

where $\varepsilon = 1 \text{ day}$ and \mathbf{I} is the identity matrix. This procedure filters modes with timescale faster than ε while leaving modes with slower timescales almost intact. $\hat{\mathbf{M}}$ can be interpreted as $\tilde{\mathbf{M}}$ averaged over time ε .

To find \mathbf{E} , we first compute the eddy fluxes for each trial using the anomalous (with respect to the climatology of each trial) daily-averaged zonal and meridional winds

and temperature on a lower resolution (every other grid-point in latitude, longitude, and pressure) for computational tractability. Results from trials with positive and negative forcings are combined to find $\langle \bar{u}'v' \rangle$ and $\langle \bar{v}'T' \rangle$, which are then projected onto the basis functions. Matrix \mathbf{Q} is calculated following the same procedure used for \mathbf{R} :

$$\mathbf{Q} = \begin{bmatrix} \langle \bar{u}'v' \rangle_1 & \langle \bar{u}'v' \rangle_2 & \cdots & \langle \bar{u}'v' \rangle_{101} & \cdots & \langle \bar{u}'v' \rangle_{200} \\ \langle \bar{v}'T' \rangle_1 & \langle \bar{v}'T' \rangle_2 & \cdots & \langle \bar{v}'T' \rangle_{101} & \cdots & \langle \bar{v}'T' \rangle_{200} \end{bmatrix} \quad (15)$$

We do not calculate \mathbf{E} using $\mathbf{Q}\mathbf{R}^{-1}$, because its large eigenvalues will be inaccurate (as discussed above) and the appropriate threshold ε for filtering similar to Eq. (14) is unclear. Instead, we use $\hat{\mathbf{M}}$, which is already filtered, as

$$\hat{\mathbf{E}} = -\mathbf{Q}(\mathbf{F}^{-1}\hat{\mathbf{M}}) \quad (16)$$

which can be interpreted as the EFM averaged over time ε .

We have not systematically attempted to optimize various aspects of the procedure such as the basis functions (10), forcing amplitudes \tilde{f}_0 (Tables S1-S2), or the filtering step (14). Still, as shown using several tests in the next section, the calculated LRF and EFM are fairly accurate and skillful.

4. Validation of the LRF and EFM

In this section we use three tests with varying degrees of complexity to examine the performance of $\hat{\mathbf{M}}$ in calculating the time-mean response to an external forcing or vice versa and compare the results with those produced using the GCM. We use the same test cases to investigate the accuracy of $\hat{\mathbf{E}}$ in computing the changes in eddy momentum and heat fluxes in response to a given change in the mean-flow (subsection 4.d).

a. Test 1: mean-flow response to an imposed Gaussian thermal forcing

First, we test the accuracy of $\hat{\mathbf{M}}$ in calculating the time-mean response $\langle \bar{\mathbf{y}} \rangle$ to a simple external thermal forcing $\tilde{f} = 0.2 \times \exp[-(p-450)^2/125^2 - (|\mu|-25)^2/15^2]$ with units of K day^{-1} . An ensemble of simulations forced with \tilde{f} is run and the ensemble-mean response is shown in Figs. 1(a)-1(b). To calculate the response from the LRF, \tilde{f} is first linearly regressed onto the 100 basis functions (10) to find a column of regression coefficients \mathbf{f} (note that the forcing is chosen so that it is not representable by a single basis function). The response is then calculated from $-\hat{\mathbf{M}}^{-1}\mathbf{f}$ as coefficients of the basis functions. The response in the grid-space is shown in Figs. 1(c)-1(d). Results show that $\hat{\mathbf{M}}$ is fairly accurate in calculating the amplitude of the response and its pattern, even at relatively small-scales. We have found $\hat{\mathbf{M}}$ similarly skillful in several other tests with thermal or mechanical Gaussian forcings.

b. Test 2: forcing needed for a given mean-flow response

In Tests 2-3, we test whether $\hat{\mathbf{M}}$ can accurately calculate the time-invariant forcing \mathbf{f} needed to achieve a complex specified time-mean response. In Test 2, the target is the time-mean response to 10% increase in the Newtonian relaxation timescale of the Held-Suarez setup. We run an ensemble using the GCM with the relaxation timescale increased to 44 days and compute $\langle \bar{\mathbf{y}} \rangle = \langle \langle \bar{\mathbf{u}} \rangle, \langle \bar{T} \rangle \rangle$, which is the target and shown in Figs. 2(a)-2(b). Time-invariant forcing needed to generate $\langle \bar{\mathbf{y}} \rangle$ in a setup with the original relaxation time of 40 days is then calculated as $\mathbf{f} = -\hat{\mathbf{M}}\langle \bar{\mathbf{y}} \rangle$ and applied in the GCM (with the original setup) to run an ensemble. The ensemble-mean response is shown in Figs. 2(c)-2(d) and agrees well, in amplitude and pattern, with the target.

c. Test 3: forcing needed to generate the Annular Mode as the mean-flow response

In Test 3, the targeted time-mean response is the positive phase of the Annular Mode of the control-run, which is calculated as the leading Empirical Orthogonal Function (EOF) of daily-averaged zonally-averaged anomalous (with respect to the climatology) zonal-wind and temperature (stacked together). The first EOF (EOF1) explains 39% of the variance and is shown in Figs. 3(a)-3(b). Using EOF1, scaled to have $\|\langle \bar{\mathbf{u}} \rangle_{\text{EOF1}}\|_{\infty} = 3 \text{ m s}^{-1}$, the time-invariant forcing is calculated as $\mathbf{f} = -\hat{\mathbf{M}} \times \text{EOF1}$ and applied in the GCM to run an ensemble. The ensemble-mean response is shown in Figs. 3(c)-3(d) and agrees well with the target.

Tests 1-3 show that the LRF $\hat{\mathbf{M}}$ is fairly skillful in calculating the pattern and amplitude of time-mean responses to external forcings and vice versa. These skills demonstrate that $\hat{\mathbf{M}}$ accurately accounts for the processes involved in the full GCM simulations and in particular the eddy-feedbacks, without which the pattern and amplitude of the forcing or response cannot be correctly captured; see section 5 and Fig. 15 of Ring and Plumb (2007) for an example. Also it should be noted that the mean-flow changes in Tests 1-3 are not negligible fractions of the mean-flow; e.g., the amplitude of the zonal-wind change in Tests 1 and 3 is $\sim 10\%$ of the maximum climatological zonal-wind ($\sim 30 \text{ m s}^{-1}$), which shows that the linear approach applies to sizable forcings and responses.

d. Validation of $\hat{\mathbf{E}}$

We use Tests 1-3 to examine the accuracy of $\hat{\mathbf{E}}$. In Fig. 4, we compare eddy fluxes ($\langle \bar{u}'v' \rangle, \langle \bar{v}'T' \rangle$) calculated from the forced GCM simulations of Tests 1-3 with those computed using Eq. (2) for ($\langle \bar{\mathbf{u}} \rangle, \langle \bar{T} \rangle$) of these simulations (see the caption for details). These results show that the EFM, $\hat{\mathbf{E}}$, is skillful in calculating the amplitude and pattern

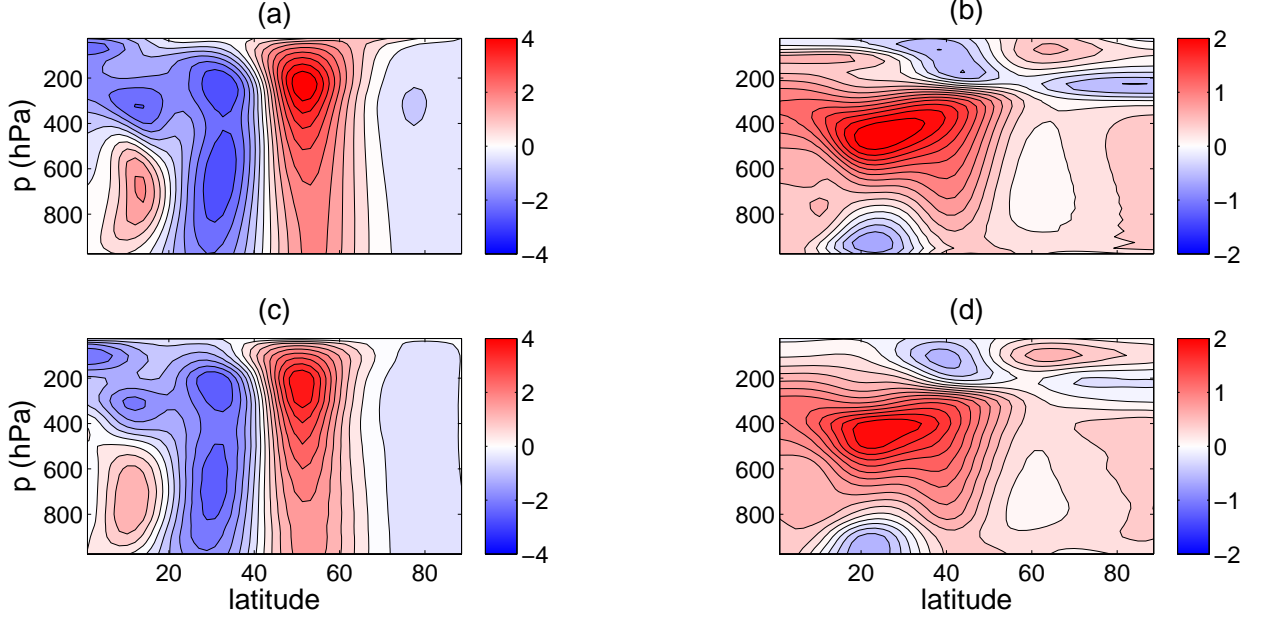


FIG. 1. Results from Test 1: time-mean response to an imposed Gaussian thermal forcing \bar{f} (see subsection 4.a for details). The ensemble-mean forced response, with respect to the ensemble-mean control-run, calculated from the GCM forced with \bar{f} is shown in (a) $\langle \bar{u} \rangle_{\text{GCM}}$ in m s^{-1} and (b) $\langle \bar{T} \rangle_{\text{GCM}}$ in K. (c) $\langle \bar{u} \rangle_{\text{LRF}}$ in m s^{-1} and (d) $\langle \bar{T} \rangle_{\text{LRF}}$ in K show the response to \bar{f} calculated using the LRF, \mathbf{M} . Employing the norms defined in Eqs. B2 and B3, relative errors are $|\|\langle \bar{u} \rangle_{\text{LRF}}\|_{\infty} - \|\langle \bar{u} \rangle_{\text{GCM}}\|_{\infty}| \times 100 / \|\langle \bar{u} \rangle_{\text{GCM}}\|_{\infty} = 14\%$, $|\|\langle \bar{T} \rangle_{\text{LRF}}\|_{\infty} - \|\langle \bar{T} \rangle_{\text{GCM}}\|_{\infty}| \times 100 / \|\langle \bar{T} \rangle_{\text{GCM}}\|_{\infty} = 8\%$, $\|\langle \bar{u} \rangle_{\text{LRF}} - \langle \bar{u} \rangle_{\text{GCM}}\|_2 \times 100 / \|\langle \bar{u} \rangle_{\text{GCM}}\|_2 = 21\%$, and $\|\langle \bar{T} \rangle_{\text{LRF}} - \langle \bar{T} \rangle_{\text{GCM}}\|_2 \times 100 / \|\langle \bar{T} \rangle_{\text{GCM}}\|_2 = 15\%$.

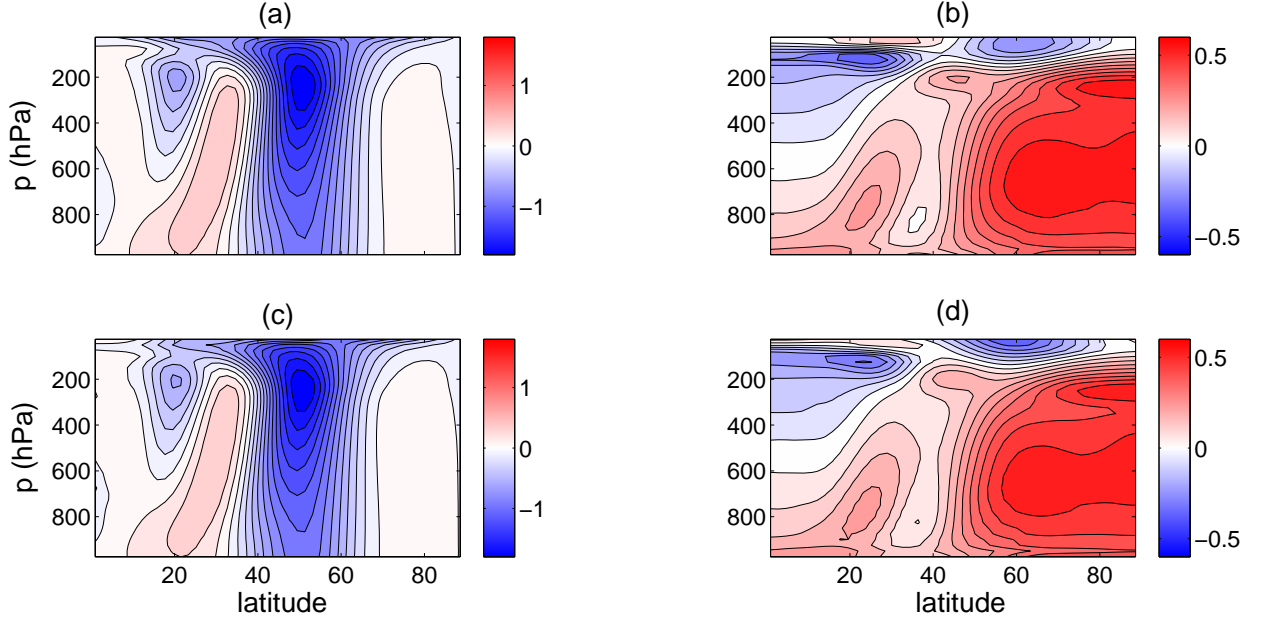


FIG. 2. Results from Test 2: forcing a specified time-mean response (target). (a) $\langle \bar{u} \rangle_{\text{GCM}}$ in m s^{-1} and (b) $\langle \bar{T} \rangle_{\text{GCM}}$ in K are the time-mean response of an ensemble GCM run with Newtonian relaxation timescale that is 10% larger than that of the control-run. (a)-(b) are the target. (c) $\langle \bar{u} \rangle_{\text{LRF}}$ in m s^{-1} and (d) $\langle \bar{T} \rangle_{\text{LRF}}$ in K are the ensemble-mean response calculated from the GCM forced with $\bar{\mathbf{f}} = -\mathbf{M} \times (\langle \bar{u} \rangle_{\text{GCM}}, \langle \bar{T} \rangle_{\text{GCM}})$ to match (a)-(b). Employing the norms defined in Eqs. B2 and B3, relative errors are $|\|\langle \bar{u} \rangle_{\text{LRF}}\|_{\infty} - \|\langle \bar{u} \rangle_{\text{GCM}}\|_{\infty}| \times 100 / \|\langle \bar{u} \rangle_{\text{GCM}}\|_{\infty} = 1\%$, $|\|\langle \bar{T} \rangle_{\text{LRF}}\|_{\infty} - \|\langle \bar{T} \rangle_{\text{GCM}}\|_{\infty}| \times 100 / \|\langle \bar{T} \rangle_{\text{GCM}}\|_{\infty} = 3\%$, $\|\langle \bar{u} \rangle_{\text{LRF}} - \langle \bar{u} \rangle_{\text{GCM}}\|_2 \times 100 / \|\langle \bar{u} \rangle_{\text{GCM}}\|_2 = 6\%$, and $\|\langle \bar{T} \rangle_{\text{LRF}} - \langle \bar{T} \rangle_{\text{GCM}}\|_2 \times 100 / \|\langle \bar{T} \rangle_{\text{GCM}}\|_2 = 8\%$.

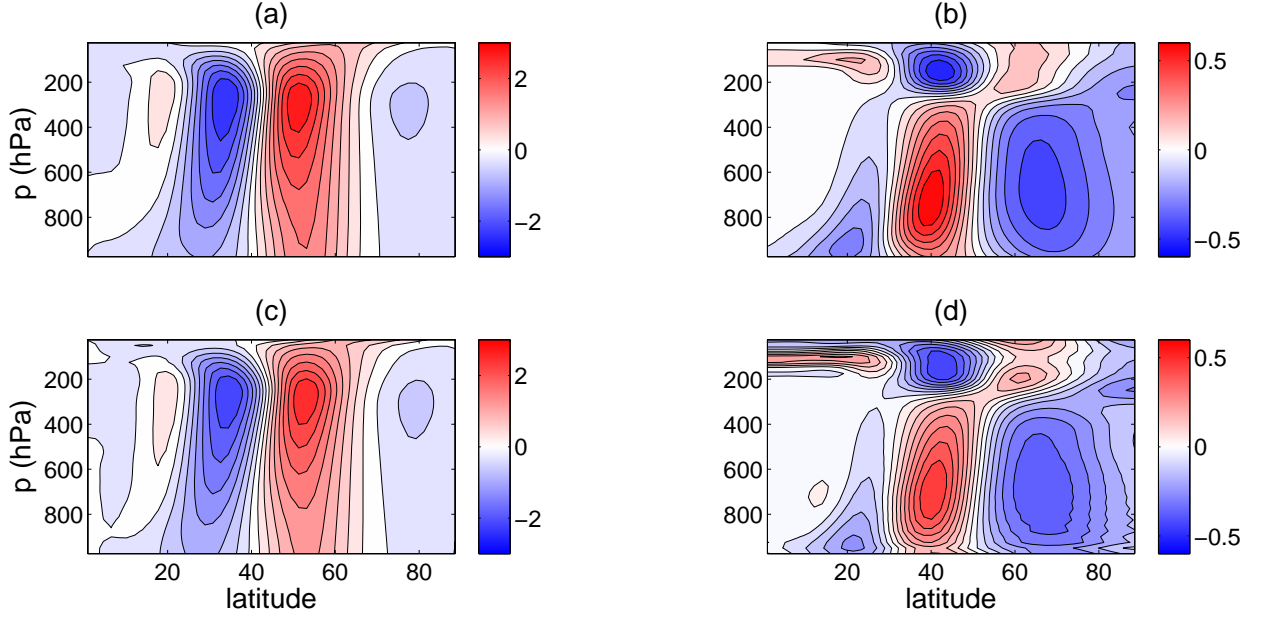


FIG. 3. Results from Test 3: forcing the positive phase of Annular Mode as the time-mean response. The first EOF (EOF1) of the control-run (a) \bar{u}_{EOF1} in m s^{-1} and (b) \bar{T}_{EOF1} in K is the target. The ensemble-mean forced response (with respect to the ensemble-mean control-run) (c) $\langle \bar{u} \rangle_{\text{LRF}}$ in m s^{-1} and (d) $\langle \bar{T} \rangle_{\text{LRF}}$ in K are calculated from the GCM forced with $\tilde{\mathbf{f}} = -\hat{\mathbf{M}} \times \text{EOF1}$ to match (a)-(b). Employing the norms defined in Eqs. B2 and B3, relative errors are $\| \langle \bar{u} \rangle_{\text{LRF}} \|_{\infty} - \| \langle \bar{u} \rangle_{\text{EOF1}} \|_{\infty} \times 100 / \| \langle \bar{u} \rangle_{\text{EOF1}} \|_{\infty} = 8\%$, $\| \langle \bar{T} \rangle_{\text{LRF}} \|_{\infty} - \| \langle \bar{T} \rangle_{\text{EOF1}} \|_{\infty} \times 100 / \| \langle \bar{T} \rangle_{\text{EOF1}} \|_{\infty} = 21\%$, $\| \langle \bar{u} \rangle_{\text{LRF}} - \langle \bar{u} \rangle_{\text{EOF1}} \|_2 \times 100 / \| \langle \bar{u} \rangle_{\text{EOF1}} \|_2 = 17\%$, and $\| \langle \bar{T} \rangle_{\text{LRF}} - \langle \bar{T} \rangle_{\text{EOF1}} \|_2 \times 100 / \| \langle \bar{T} \rangle_{\text{EOF1}} \|_2 = 23\%$.

of the eddy flux time-mean response to a given change in the mean-flow.

5. Singular Value and Eigenvalue Decompositions

Results of section 4 validate $\hat{\mathbf{M}}$ as the accurate LRF of the idealized dry atmosphere. An important piece of information that can be obtained from $\hat{\mathbf{M}}$ is the dynamical mode with the largest response to imposed forcings. The problem can be formulated as finding the maximum of $\{ \langle \bar{\mathbf{y}} \rangle, \langle \bar{\mathbf{y}} \rangle \} / \{ \langle \bar{\mathbf{f}} \rangle, \langle \bar{\mathbf{f}} \rangle \}$ where $\{ \cdot \}$ is the inner product. It follows from Eq. (9) that

$$\begin{aligned} \frac{\{ \langle \bar{\mathbf{y}} \rangle, \langle \bar{\mathbf{y}} \rangle \}}{\{ \langle \bar{\mathbf{f}} \rangle, \langle \bar{\mathbf{f}} \rangle \}} &= \frac{\{ \langle \bar{\mathbf{y}} \rangle, \langle \bar{\mathbf{y}} \rangle \}}{\{ \hat{\mathbf{M}} \langle \bar{\mathbf{y}} \rangle, \hat{\mathbf{M}} \langle \bar{\mathbf{y}} \rangle \}} = \frac{\{ \langle \bar{\mathbf{y}} \rangle, \langle \bar{\mathbf{y}} \rangle \}}{\{ \tilde{\mathbf{M}}^{\dagger} \tilde{\mathbf{M}} \langle \bar{\mathbf{y}} \rangle, \langle \bar{\mathbf{y}} \rangle \}} \\ &= \frac{\{ \langle \bar{\mathbf{y}} \rangle_m, \langle \bar{\mathbf{y}} \rangle_m \}}{\{ \tilde{\mathbf{M}}^{\dagger} \tilde{\mathbf{M}} \langle \bar{\mathbf{y}} \rangle_m, \langle \bar{\mathbf{y}} \rangle_m \}} = \frac{\{ \langle \bar{\mathbf{y}} \rangle_m, \langle \bar{\mathbf{y}} \rangle_m \}}{\{ s_m^2 \langle \bar{\mathbf{y}} \rangle_m, \langle \bar{\mathbf{y}} \rangle_m \}} \end{aligned} \quad (17)$$

where \dagger denotes the adjoint, and $\langle \bar{\mathbf{y}} \rangle_m$ is the m^{th} eigenvector of $\tilde{\mathbf{M}}^{\dagger} \tilde{\mathbf{M}}$ with eigenvalue s_m^2 . It is evident from Eq. (17) that the maximum response is the eigenvector with the smallest eigenvalue, which is in fact the right singular vector of $\hat{\mathbf{M}}$ with smallest singular number s_m , and is sometimes referred to as the neutral vector of the system (Marshall and Molteni 1993; Goodman and Marshall 2002). The dynamical significance of the neutral vector is that

it is the largest response to forcings imposed on the atmosphere, and is therefore expected to be a prevailing component of the response to climate change-induced forcings as well as of the pattern of the low-frequency internal variability, because as discussed in section 2, $\tilde{\mathbf{f}}$ can represent the stochastic eddy forcing due to the internal atmospheric dynamics as well. See Palmer (1999), Palmer and Zanna (2013), Farrell and Ioannou (1996a,b), and Goodman and Marshall (2002) for further discussions on the significance of the singular vectors of the LRF.

The neutral vector of $\hat{\mathbf{M}}$ (and of $\tilde{\mathbf{M}}$), calculated using a singular value decomposition, is shown in Fig. 5. The zonal-wind of the neutral vector is dipolar and equivalent-barotropic and strongly resembles the zonal-wind component of EOF1 (Fig. 3(a)). This explains the dominance of Annular Mode-like patterns in the response of zonal-wind in this model to various mechanical and thermal forcings (e.g., Ring and Plumb 2007; Butler et al. 2010, also see Fig. B1). These results further support the findings of Ring and Plumb (2008) that the Annular Mode is truly a dynamical mode of the system rather than just a variability pattern obtained through statistical analysis. The connection between the neutral vector and EOF1 has been discussed previously in Navarra (1993), Goodman and Marshall (2002), and Kuang (2004). In particular, as shown in Goodman and Marshall (2002, Eqs. 10-12), the neutral vector and EOF1 are identical if the stochas-

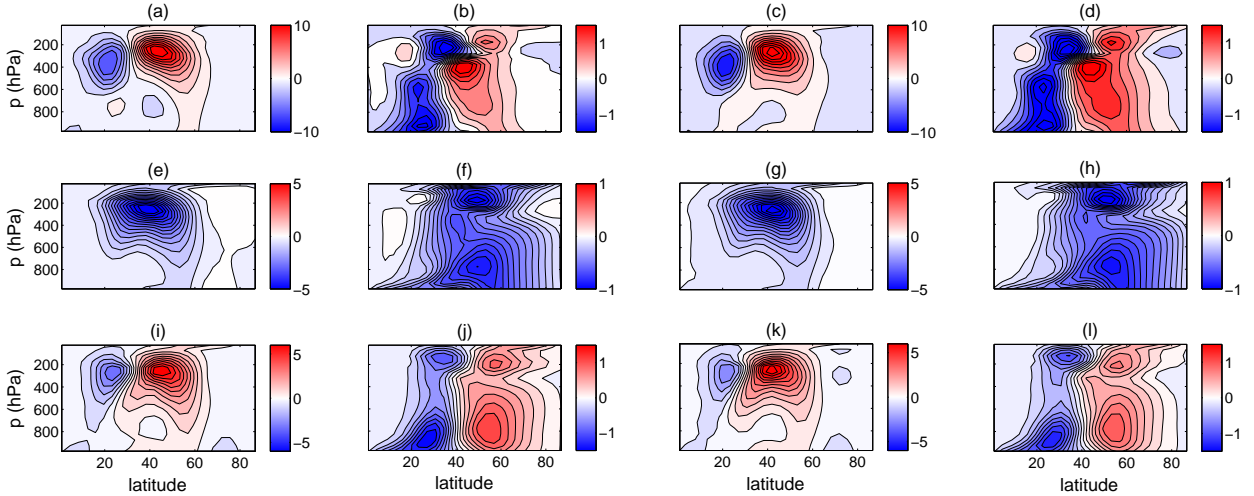


FIG. 4. Changes in time-mean eddy fluxes calculated using the GCM (two left columns) and EFM (two right columns) for Tests 1-3. From the left, the first and third (second and fourth) columns show eddy momentum (heat) fluxes $\langle u'v' \rangle$ ($\langle v'T' \rangle$) with units $\text{m}^2 \text{s}^{-2}$ (K m s^{-1}). Test 1: (a)-(b) show the ensemble-mean eddy fluxes response to the forcing calculated from the GCM. (c)-(d) show the eddy fluxes response calculated using $\hat{\mathbf{E}}$ and the ensemble-mean $(\langle \bar{u} \rangle, \langle \bar{T} \rangle)$ of the forced GCM runs (shown in Figs. 1(a)-1(b)). Relative errors in amplitude are $\| \langle u'v' \rangle_{\text{EMF}} - \langle u'v' \rangle_{\text{GCM}} \|_{\infty} \times 100 / \| \langle u'v' \rangle_{\text{GCM}} \|_{\infty} = 27\%$ and $\| \langle v'T' \rangle_{\text{EMF}} - \langle v'T' \rangle_{\text{GCM}} \|_{\infty} \times 100 / \| \langle v'T' \rangle_{\text{GCM}} \|_{\infty} = 25\%$. Test 2: (e)-(f) show the ensemble-mean eddy fluxes response calculated from the GCM simulations with increased Newtonian relaxation time. (g)-(h) show the eddy fluxes response calculated using $\hat{\mathbf{E}}$ and the ensemble-mean $(\langle \bar{u} \rangle, \langle \bar{T} \rangle)$ of these GCM simulations (shown in Figs. 2(a)-2(b)). Relative errors in amplitude are 4% and 3% for the momentum and heat fluxes, respectively. Test 3: (i)-(j) show the ensemble-mean eddy fluxes response calculated from the forced GCM runs. (k)-(l) show the eddy fluxes response calculated using $\hat{\mathbf{E}}$ and the ensemble-mean $(\langle \bar{u} \rangle, \langle \bar{T} \rangle)$ of these forced GCM simulations (shown in Figs. 3(c)-3(d)). Relative errors in amplitude are 13% and 11% for the momentum and heat fluxes, respectively.

tic eddy forcing is spatially uncorrelated and has uniform variance everywhere, i.e., $\langle \tilde{\mathbf{f}} \tilde{\mathbf{f}}^\dagger \rangle = \mathbf{I}$ if $\tilde{\mathbf{f}}$ has unit amplitude. The zonal-wind pattern of the neutral vector (Fig. 5(a)) is certainly very similar to the zonal-wind pattern of EOF1 (Fig. 3(a)), with the exception of small differences in the stratosphere around 40° . The temperature patterns, however, are in general different except in the midlatitude around $30^\circ - 50^\circ$.

The above calculations of singular vectors are subject to uncertainties in the relative weights used for the different variables (e.g., zonal-wind versus temperature), or in other words, the choice of norm (Kuang 2004). However, below we show that the difference between the neutral vector of $\hat{\mathbf{M}}$ and EOF1 in our results is mostly due to fact that the stochastic eddy forcing is not isotropic and uncorrelated and therefore does not satisfy the above condition. This is demonstrated by calculating the EOF1 of $\bar{\mathbf{z}}$ obtained from a long integration of the stochastic linear equation $\dot{\bar{\mathbf{z}}} = \hat{\mathbf{M}}\bar{\mathbf{z}} + \boldsymbol{\zeta}$, where $\boldsymbol{\zeta}(t)$ is Gaussian white noise ($\langle \boldsymbol{\zeta} \boldsymbol{\zeta}^\dagger \rangle = \mathbf{I}$). For this case the conditions on the forcing are satisfied and the EOF1 is almost identical to the neutral vector of $\hat{\mathbf{M}}$ in both zonal-wind and temperature patterns (see Fig. S2).

We further highlight that despite various simplifications in the idealized GCM used here, the pattern of the Annular Mode in this model (i.e., the EOF1 shown in Fig. 3(a)-3(b)) resembles the observed patterns of the

Northern Annular Mode (NAM) (Thompson and Li 2015, Fig. 2) and the Southern Annular Mode (SAM) (Thompson and Woodworth 2014, Fig. 2) particularly for zonal-winds (also note that the details of EOF calculation in the current study are different from those in the two aforementioned papers; here the EOF is calculated from extended EOF analysis of unweighted (\bar{u}, \bar{T})). These similarities and the above discussion on the connection between neutral vector and EOF1 suggest that it is plausible that the neutral vector of the extratropical atmospheric circulation in more complex GCMs and the real atmosphere resembles the patterns in Fig. 5 particularly for the zonal-wind, which would explain the ubiquity of Annular Mode-like patterns in the midlatitude response to external forcings in full-physics GCM (e.g., Peings and Magnusdottir 2014; Deser et al. 2015).

We also briefly discuss the eigenmodes of $\hat{\mathbf{M}}$ (the eigenmodes of $\hat{\mathbf{M}}$ are similar with slightly reduced eigenvalues due to the filtering (14)). In Fig. S1 we show the eigenvalues of $\hat{\mathbf{M}}$ with timescales longer than 1 day, which are all decaying and the slowest decaying modes have timescales on the order of tens of days. Selected eigenvectors of the slowest decaying modes are shown in Fig. S3. The zonal-wind and temperature of the slowest decaying eigenvector are mostly confined to the stratosphere, although there is a weak Annular Mode signature in the troposphere. The decaying timescale is ~ 59 days, which is comparable to

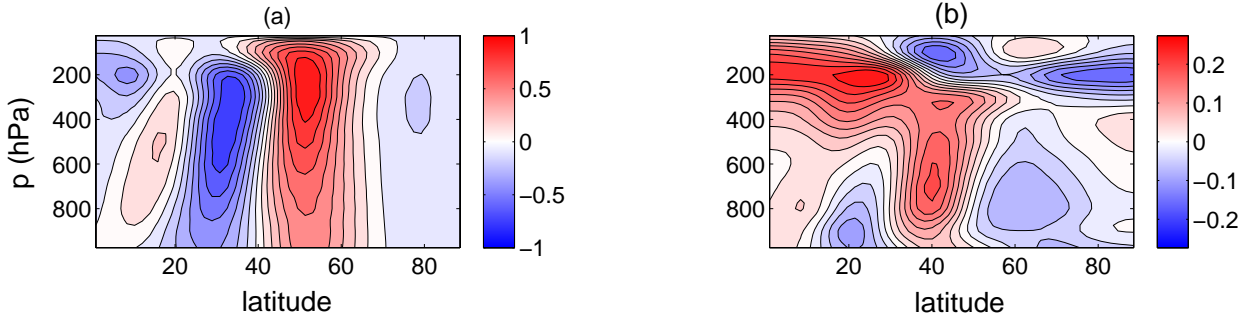


FIG. 5. The neutral vector of $\hat{\mathbf{M}}$: (a) zonal-wind in m s^{-1} and (b) temperature in K. The neutral vector is calculated as the right singular vector of $\hat{\mathbf{M}}$ with the smallest singular number, and is rescaled to have $\|\bar{\mathbf{u}}\|_{\infty} = 1 \text{ m s}^{-1}$. The neutral vector of $\hat{\mathbf{M}}$ is indistinguishable from the pattern shown here.

the imposed 40-day Newtonian relaxation time. The next few slowest decaying modes have timescales ~ 30 days or shorter and zonal-wind patterns with strong Annular Mode signatures.

6. Applications of the LRF and EFM

In this section we briefly discuss some of the potential applications of $\hat{\mathbf{M}}$ and $\hat{\mathbf{E}}$ which can be categorized as i) forcing a specified mean-flow for hypothesis-testing, ii) isolating and quantifying eddy-feedbacks, and iii) examining and evaluating more generally-applicable methods.

One difficulty in fully understanding the dynamics of many complex atmospheric phenomena even using extensive GCM experiments is that several changes in the large-scale circulation, such as the speed and latitude of the jet-streams and static stability, might happen simultaneously in response to a forcing or varying a physical parameter, which obscure understanding the direction of causation and the individual contribution of each change. This problem exists even in idealized GCMs such as the one used here, and common but imperfect remedies include nudging and/or tuning the forcing to control the changes in the large-scale circulation (Kidston et al. 2011; Simpson et al. 2013a; Garfinkel et al. 2013). The LRF can be used to accurately calculate time-invariant forcings needed to generate a desired mean-flow (as done in Tests 2-3) and use the well-controlled experiments to disentangle the influences of different changes in the mean-flow on the phenomenon under study.

For example, in Hassanzadeh and Kuang (2015), we used the LRF to examine causality in the relationship between the negative phase of NAM and increased atmospheric blocking, which is seen in observational data and GCM simulations, including the idealized GCM used here. To test whether the mean-state of the negative phase of NAM (i.e., the patterns in Figs. 3(a)-(b) with opposite signs) causes more blocking, $\hat{\mathbf{M}}$ was used to force this mean-state with various amplitudes (similar to Test 3), and

it was found that blocking decreases as the amplitudes increases. Results suggest that the observed blocking-NAM relationship is a correlation which does not imply that the mean-state of the negative phase of NAM causes more blocking. These findings have important implications for the ongoing debate on the linkage between Arctic Amplification and the midlatitude weather extremes (see, e.g., Hassanzadeh et al. 2014; Barnes and Screen 2015).

As discussed in section 1, isolating and quantifying the eddy-feedbacks is another difficulty in developing a full mechanistic understanding of problems in which eddy-mean flow interaction plays an important role; examples of such problems include the dynamics of the Annular Modes and their overestimated persistence in GCMs (Feldstein and Lee 1998; Robinson 2000; Lorenz and Hartmann 2001; Simpson et al. 2013a; Nie et al. 2014), poleward shift of the midlatitude jets under climate change (Chen and Held 2007; Kidston et al. 2011; Lorenz 2014) and troposphere-stratosphere coupling (Kushner and Polvani 2004; Song and Robinson 2004; Domeisen et al. 2013). The EFM $\hat{\mathbf{E}}$ and similar matrices for eddy-phase speed and eddy length-scale can be used to isolate and quantify the response of eddies to a given change in the mean-flow, which combined with well-controlled GCM experiments made possible using $\hat{\mathbf{M}}$, can help with developing a deeper dynamical understanding of these problems.

A limitation of the approach presented here is that to study various problems involving different physical processes, LRF and EFM should be recalculated for GCMs that represent these processes. However, it should be highlighted that the dry dynamical core with Held-Suarez physics is a widely-used GCM that provides a dynamical framework to study the role of dry processes in various complex problems. Thus the calculated LRF and EFM can be used to study a variety of problems (some mentioned above). Furthermore, the approach presented in this paper can be applied to construct the LRFs and EMFs for more complex GCMs and for zonally-asymmetric forcings/responses. For more complex GCMs, the main dif-

ficulty will be likely the computational cost associated with the larger size of the state-vector (i.e., number of variables) and achieving a reasonable signal-to-noise ratio in the linear regime. Note that for zonally-asymmetric forcing/responses, it might be better to use basis functions that are vertically in grid-space (used here in both directions) but horizontally in spectral-space (i.e., use low-wavenumber spherical harmonics).

Additionally, the LRF and EFM constructed here can be used to evaluate, complement, and potentially improve generally-applicable methods that are currently employed to construct LRFs and quantify eddy-feedbacks in the outputs of idealized and comprehensive GCMs. Such methods include FDT, to construct LRFs, and lag-regression (Lorenz and Hartmann 2001; Simpson et al. 2013b) and finite-amplitude wave-activity (Nakamura and Zhu 2010; Nie et al. 2014), to diagnose eddy feedbacks. As an example, in the next section, we use $\tilde{\mathbf{M}}$ to investigate why the LRF constructed using the FDT performs poorly in some cases.

7. The Fluctuation-Dissipation Theorem (FDT)

In statistical physics, the FDT relates the mean-response of a nonlinear system to weak external forcing with the internal variability of the system (see Marconi et al. 2008, for a review). Leith (1975) introduced the FDT to the climate science, argued that the climate system approximately satisfies the conditions for the theorem to hold, and formulated how the LRF in Eq. (9) can be calculated only using the covariance and lag-covariances of the unforced system (see below). Since then many studies have used climate models of varying degrees of complexity to examine the LRFs calculated using different forms of FDT and the implications of this theorem (e.g., Bell 1980; North et al. 1993; Cionni et al. 2004; Gritsun and Branstator 2007; Abramov and Majda 2007; Gritsun et al. 2008; Ring and Plumb 2008; Gerber et al. 2008a,b; Majda et al. 2010; Gershgorin and Majda 2010; Achatz et al. 2013; Lutsko et al. 2015; Fuchs et al. 2015). However, the competency of the FDT for the climate system remains unclear as some of these studies found FDT to only work qualitatively, although some other, such as Gritsun and Branstator (2007) and Fuchs et al. (2015) found promising quantitative skills.

How accurately the FDT holds for the climate system is important, not only because of the possibility to construct skillful LRFs from unforced GCM simulations or even ambitiously, from observational records, but also because some of the implications of this theorem. For example, FDT relates the amplitude of the forced response to the timescales of internal modes of variability of the system (e.g., Ring and Plumb 2008; Shepherd 2014). Given that idealized and comprehensive GCMs overestimate the persistence of the Annular Modes in both hemispheres by

factors as large as 2–3 (and even larger in some cases), an important implication of FDT is that these models also overestimate the mean-response to external forcings by such factors, which has significant consequences for climate sensitivity (Shepherd 2014; Gerber et al. 2008a,b; Ring and Plumb 2008).

a. Formulation of the FDT

According to the most common formulation, the so-called quasi-Gaussian FDT, the LRF $\tilde{\mathbf{M}}_{\text{FDT}}$ that relates the mean-response $\langle \bar{\mathbf{y}} \rangle$ to an imposed forcing $\langle \bar{\mathbf{f}} \rangle$ via Eq. (9) can be calculated as

$$\tilde{\mathbf{M}}_{\text{FDT}} = - \left[\int_0^\infty \mathbf{C}(\tau) \mathbf{C}(0)^{-1} d\tau \right]^{-1} \quad (18)$$

where $\mathbf{C}(\tau) = \langle \mathbf{y}(\tau) \mathbf{y}(0)^\dagger \rangle$ is the lag- τ covariance matrix. Recently, Majda et al. (2005) and Gritsun and Branstator (2007) have demonstrated that Eq. (18) can be derived under conditions that are more closely satisfied by the atmosphere compared to those used by Leith (1975) and Kraichnan (1959). Still, an important assumption involved in (18) is that $\bar{\mathbf{y}}$ has Gaussian statistics; however, non-Gaussianity in dynamical and thermodynamic variables has been found in observational data (e.g., Ruff and Neelin 2012; Huybers et al. 2014; Loikith and Neelin 2015) and GCM simulations (e.g., Berner and Branstator 2007; Franzke et al. 2007; Sardeshmukh and Sura 2009; Hassanzadeh et al. 2014).

Furthermore, there are practical problems with calculating $\tilde{\mathbf{M}}_{\text{FDT}}$ in Eq. (18) generally due to the limited length of the dataset. Realistically, the upper bound of the integral is replaced with a finite number τ_∞ and while a small τ_∞ degrades the approximation of the integral, a large τ_∞ can lead to an imprecise $\tilde{\mathbf{M}}_{\text{FDT}}$ because of inaccuracies in \mathbf{C} at large τ due to limited sample size. Additionally, the calculation of $\tilde{\mathbf{M}}_{\text{FDT}}$ or $\tilde{\mathbf{M}}_{\text{FDT}}^{-1}$ involves the inverse of the sum of the lag-covariance matrices or $\mathbf{C}(0)^{-1}$. These matrices can be close to singular because of short datasets and anisotropic internal fluctuations, which together result in the phase-space not being entirely excited by the fluctuations. The common remedy for this problem is to calculate \mathbf{C} and $\tilde{\mathbf{M}}_{\text{FDT}}$ on reduced dimensions, e.g., by first projecting the data onto a specified number (n_{EOF}) of the leading EOFs (Penland 1989; Gritsun and Branstator 2007; Ring and Plumb 2008). Another practical issue is the number of variables that are included in the state-vector $\bar{\mathbf{y}}$. Some studies have used one variable such as zonal-wind or temperature and some other have used two or more variables.

It is plausible that the reported inaccuracies in FDT and discrepancy in the previous studies are due to, among others, non-Gaussianity in the data as well as practical problems such as short datasets and uncertainties in choosing τ_∞ , n_{EOF} , and $\bar{\mathbf{y}}$. Several interesting studies have recently attempted to systematically address the issues related to

sample size and dimension-reduction in calculations of \mathbf{C} (Fuchs et al. 2015; Lutsko et al. 2015; Cooper et al. 2013), state-vector reduction (Majda et al. 2010), and non-Gaussianity (Cooper et al. 2013); however, further work is evidently needed to fully utilize the FDT for practical applications.

To further evaluate the performance of LRFs calculated from FDT and to better understand the potential sources of their inaccuracies, in subsection 7.b we have employed multivariate FDT and a long dataset to compute $\tilde{\mathbf{M}}_{\text{FDT}}$ for the idealized GCM and have tested its performance using the tests of section 4. In subsections 7.c and 7.d we show, using $\hat{\mathbf{M}}$ and examples of 2×2 matrices, that the dimension-reduction using the leading EFOs can alone be a major source of inaccuracy in $\tilde{\mathbf{M}}_{\text{FDT}}$ for systems with non-normal operators, which are common in the atmosphere and ocean.

b. Tests 1 – 3 for $\tilde{\mathbf{M}}_{\text{FDT}}$

For the same control-run setup described in section 3.a, we have constructed $\tilde{\mathbf{M}}_{\text{FDT}}$ from Eq. (18) using a one million-day dataset and have used Tests 1 – 3 (section 4) to evaluate its performance. To find the best performance of $\tilde{\mathbf{M}}_{\text{FDT}}$, for each Test we have tried $\tau_{\infty} = 20, 30, 45, 60$, and 90 days and $n_{\text{EOF}} = 64$ (97.5%), 113 (99.0%), 165 (99.5%), 200 (99.7%), and 300 (99.8%) where the parentheses show the explained variance. To minimize the computational cost given the large combination of $(\tau_{\infty}, n_{\text{EOF}})$, we have first used $\hat{\mathbf{M}}$ instead of the GCM for Tests 2 and 3 to find the best performance of $\tilde{\mathbf{M}}_{\text{FDT}}$; the GCM is only used for the selected $(\tau_{\infty}, n_{\text{EOF}})$. Following the analysis of section 2 and Appendix A, we use $\bar{\mathbf{y}} = (\bar{\mathbf{u}}, \bar{T})$. An ensemble of 10 unforced simulations, each 50000 days, are used to create the employed dataset, which contains daily-averaged anomalous $\bar{\mathbf{u}}$ and \bar{T} of the last 49500 days of each simulation where each variable is weighted by $\sqrt{\cos \mu}$ and normalized by area-averaged standard deviation of each vertical level p (we did not find the performance of FDT sensitive to the weighting details). Covariance matrices are then calculated for each hemisphere of each simulation from $(\bar{\mathbf{u}}, \bar{T})$ (stacked together). The 20 covariance matrices are subsequently averaged to calculate the EOFs of the ensemble. Then, the weighted daily-averaged anomalous $(\bar{\mathbf{u}}, \bar{T})$ is projected onto the first n_{EOF} EOFs using least-square linear regression, and the results are used to calculate the reduced-dimension covariance and lag-covariance matrices for each hemisphere in each simulation, which are then averaged for each τ to find $\mathbf{C}(\tau)$ for $\tau = 0, 1, 2, \dots, 90$ days. The integral in (18) is evaluated using the trapezoidal rule.

The mean-response to the Gaussian thermal forcing of Test 1 calculated using $\tilde{\mathbf{M}}_{\text{FDT}}$ is shown in Figs. 6(a)-6(b). Comparing with the true response (Figs. 1(a)-1(b)) shows that while $\tilde{\mathbf{M}}_{\text{FDT}}$ can crudely reproduce the patterns of the

zonal-wind and temperature response such as the poleward shift of the jet and warming in the subtropical mid-troposphere, it cannot reproduce the amplitude of the response or its patterns at small-scales. We have further tested the performance of $\tilde{\mathbf{M}}_{\text{FDT}}$ using a similar Gaussian thermal forcing but at $(\mu_o, p_o) = (0, 300)$ (the true mean-response is shown in Fig. S4). The mean-response calculated using $\tilde{\mathbf{M}}_{\text{FDT}}$ (Figs. 6(c)-6(d)) agrees better, both qualitatively and quantitatively, with the true response compared to Test 1, but there are still notable differences particularly in the zonal-wind. For Tests 2 and 3, the mean-responses in zonal-wind and temperature, obtained in a similar way as Figs. 2(c)-2(d) and Figs. 3(c)-3(d) but with $\tilde{\mathbf{M}}_{\text{FDT}}$ instead of $\hat{\mathbf{M}}$, are shown in Figs. 6(e)-6(f) and 6(g)-6(h), respectively. For Test 2, $\tilde{\mathbf{M}}_{\text{FDT}}$ reproduces the zonal-wind response fairly well both qualitatively and quantitatively except in the tropical stratosphere. The pattern and amplitude of the temperature response, however, are poorly reproduced using $\tilde{\mathbf{M}}_{\text{FDT}}$. For Test 3, both zonal-wind and temperature responses are reproduced reasonably well using $\tilde{\mathbf{M}}_{\text{FDT}}$ with the exception of the pattern of the temperature response at high-latitudes. It should be highlighted that in all these tests, the best results are obtained with $\tau_{\infty} = 30$ days, which is around the decorrelation time of EOF1 in the control-run. Gritsun and Branstator (2007) and Fuchs et al. (2015) also used $\tau_{\infty} = 30$ days, although their GCMs and setups are very different from ours. Whether this is a coincidence or choosing τ_{∞} around the decorrelation time of the EOF1 of the model yields the best results with limited sample size merits further investigation.

The results of Fig. 6 show that the LRF calculated using the FDT is relatively accurate for some problems, such as Test 1 with the tropical forcing and Test 3, and inaccurate and only qualitative for some other, such as Test 1 with subtropical forcing and Test 2, consistent with the findings of previous studies (e.g., Gritsun and Branstator 2007; Lutsko et al. 2015; Fuchs et al. 2015). However, even in Test 3 where the FDT performs the best, some features of the response, such as cooling in the high-latitudes, are poorly reproduced, which can limit applications of $\tilde{\mathbf{M}}_{\text{FDT}}$, for example for hypothesis-testing.

The source(s) of the poor performance of $\tilde{\mathbf{M}}_{\text{FDT}}$ for some problems and its inability to reproduce some patterns of the response is unclear and difficult to identify and might be due to violation of the assumptions underlying Eq. (18) such as Gaussianity and/or one or some of the practical issues discussed in subsection 7.a. The departure from Gaussianity in the control-run is found to be substantial in particular for temperature for which the skewness and kurtosis of daily averages can be as large as 2 and 14, respectively. Although we use the equivalent of a 990000-day integration to compute $\tilde{\mathbf{M}}_{\text{FDT}}$, the limited dataset can certainly still be a source of error. However, the results shown in Fig. 6 are not substantially better than

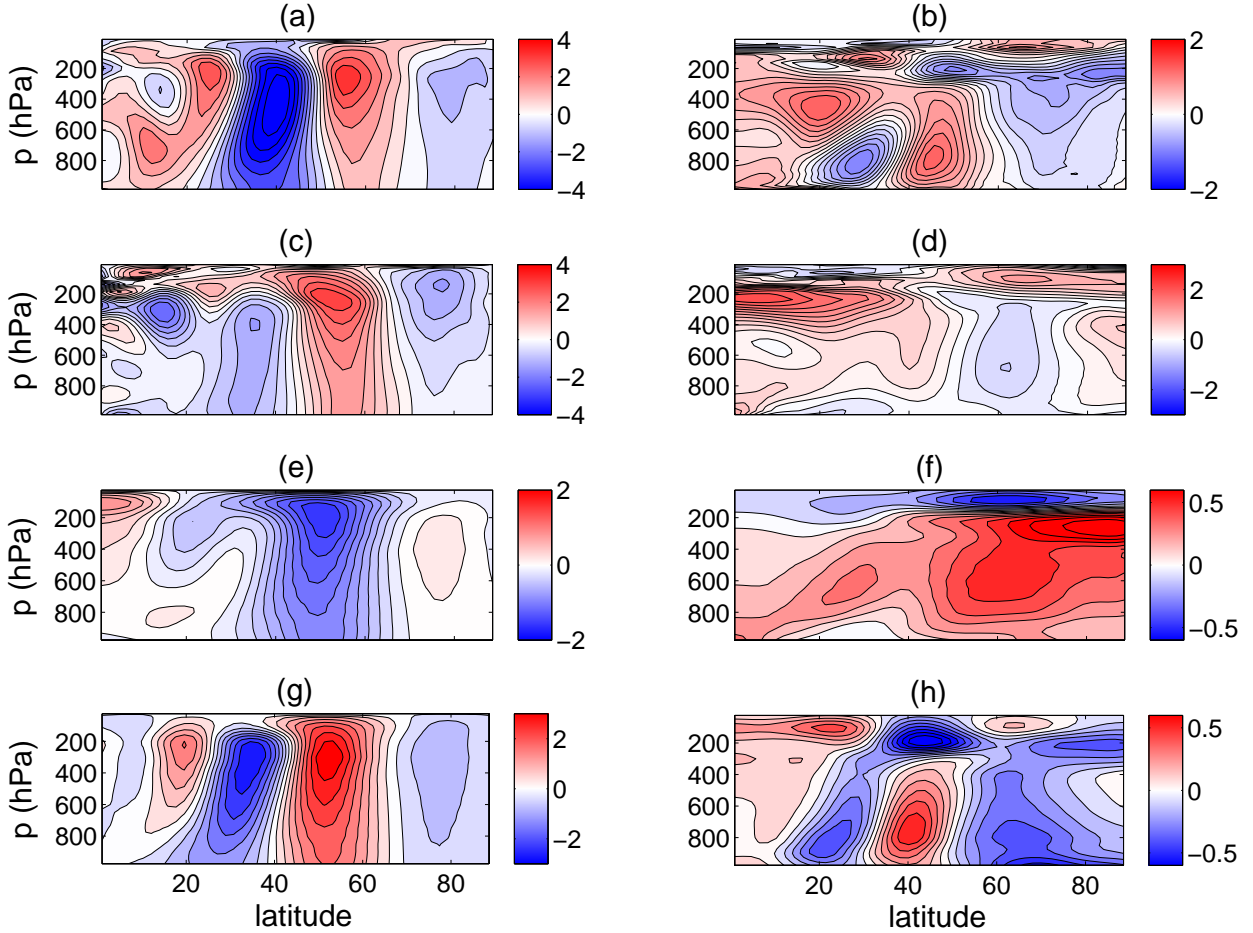


FIG. 6. Tests 1 – 3 for $\tilde{\mathbf{M}}_{\text{FDT}}$. For each Test, the best results for the attempted ranges of τ_∞ and n_{EOF} are shown. The left (right) panels show the time-mean zonal-wind in m s^{-1} (temperature in K). (a)–(b) Test 1; the relative errors in amplitude are 21% and 31%, respectively. (c)–(d) similar to Test 1 but for tropical forcing $\bar{f} = 0.2 \times \exp[-(p - 300)^2/100^2 - \mu^2/20^2]$; the relative errors in amplitude are 6% and 24%, respectively. Results of (a)–(d) are obtained with $\tau_\infty = 30$ days and $n_{\text{EOF}} = 165$. (e)–(f) Test 2; the relative errors in amplitude are 14% and 44%, respectively. (g)–(h) Test 3; the relative errors in amplitude are 13% and 14%, respectively. Results of (e)–(h) are obtained with $\tau_\infty = 30$ days and $n_{\text{EOF}} = 200$.

those obtained using only one fifth of the dataset (but it should be noted that the error in $\tilde{\mathbf{M}}_{\text{FDT}}$ decreases as $1/\sqrt{N}$ with the length of the dataset N (Gritsun and Branstator 2007)). Nonlinearity and state-vector reduction are likely not the sources of the poor performance of $\tilde{\mathbf{M}}_{\text{FDT}}$ given the good performance of $\hat{\mathbf{M}}$ for these tests (section 4) and the state-vector reduction analysis of Appendix A.

The dimension-reduction using projection onto a number of the leading EOFs is another likely source of error. For example, Gritsun and Branstator (2007) and Fuchs et al. (2015) have found that the LRFs calculated using the FDT perform poorly when the forcings project onto the excluded EOFs. This happens when the forcing pattern differs significantly from the leading EOFs, which is the case for Gaussian forcings. In the following two subsections, we show that the dimension-reduction alone can result in a significantly poor performance of $\tilde{\mathbf{M}}_{\text{FDT}}$ for systems with

non-normal LRFs, and that the errors increase rapidly with non-normality. This non-normality, not to be confused with non-Gaussianity of the statistics of the state-vector, refers to the non-orthogonality of the eigenvectors of the operator \mathbf{A} (Farrell and Ioannou 1996a,b; Trefethen et al. 1993; Butler and Farrell 1992; Reddy et al. 1993) and can result in strong interaction between the components of the forcing and response that project onto the included (resolved) and excluded (unresolved) EOFs.

c. Tests using a linear stochastic equation with $\hat{\mathbf{M}}$

To focus on the effect of dimension-reduction and eliminate other possible causes for a poor performance of the LRF calculated using FDT, we use a dataset that consist of daily-averaged $\bar{\mathbf{z}}$ obtained from integrating the linear

stochastic equation

$$\dot{\bar{\mathbf{z}}} = \hat{\mathbf{M}}\bar{\mathbf{z}} + \zeta \quad (19)$$

using the Euler-Maruyama method (Higham 2001) with a 0.1 day timestep for 15 million days. $\bar{\mathbf{z}}$ is a 200×1 state-vector consisting of the coefficients of basis functions (10) for (\bar{u}, \bar{T}) (similar to $\bar{\mathbf{y}}$), and $\zeta(t)$ is a 200×1 vector of Gaussian white noise. The advantage of investigating FDT using (19) is that while its LRF has the same complexity as that of the GCM, the problem is linear, it produces Gaussian statistics, it can be easily integrated to generate a very long dataset, and the noise is uniformly added to excite all basis functions. As a result of the last two, $\mathbf{C}(\tau)$ can be accurately calculated for large τ , and $\mathbf{C}(0)^{-1}$ and $[\int \mathbf{C}(\tau) d\tau]^{-1}$ can be computed without the need for dimension-reduction.

Similar to the procedure used previously, $\bar{\mathbf{z}}$ normalized with the standard deviation of each pressure level is used to calculate $\mathbf{C}(\tau)$ for $\tau = 0, 1, \dots, 90$ days, which are then used to compute $\hat{\mathbf{M}}_{\text{FDT}}$ from (18). The mean-responses to a unit-amplitude thermal forcing of the basis function at $(\mu_o, p_o) = (30^\circ, 400 \text{ hPa})$ calculated using $\hat{\mathbf{M}}$ (the true response) and $\hat{\mathbf{M}}_{\text{FDT}}$ (obtained without dimension-reduction) are shown in Figs. 7(a)-7(d). The amplitude and patterns of the two responses agree well. When $\hat{\mathbf{M}}_{\text{FDT}}$ is calculated with dimension-reduction using the first 81 EOFs (which explain 90% of the variance), the performance of FDT declines significantly (Figs. 7(e)-7(f)) and relative errors in amplitude as large as 60% arise.

The errors are not simply due to the inability of the dimension-reduced $\hat{\mathbf{M}}_{\text{FDT}}$ to capture part of the true response that projects onto the *unresolved* EOFs and is forced by the *unresolved* component of the forcing (i.e., components of forcing that projects onto the excluded EOFs). In fact similar differences in pattern and errors in amplitude are found if only parts of the responses that project onto the first 81 EOFs are compared (see the caption). Therefore, the error is due to the inability of the dimension-reduced $\hat{\mathbf{M}}_{\text{FDT}}$ to capture part of the true response that projects onto the *resolved* EOFs and is forced by the *unresolved* component of the forcing. This component of the response, which depends on the non-normality of the LRF, can complicate understanding the relationship between the error in the predicted response and the unresolved part of the forcing, and can be best understood using simple examples of 2×2 matrices.

d. Tests using 2×2 normal and non-normal matrices

We focus on a simple linear system

$$\dot{\mathbf{z}} = \mathbf{A}\mathbf{z} + \zeta + \mathbf{f} \quad (20)$$

where $\mathbf{z} = (z_1, z_2)$ is a 2×1 state-vector and $\zeta(t)$ and \mathbf{f} are 2×1 vectors of Gaussian white noise and time-invariant

external forcing, respectively. To start, we choose \mathbf{A} to be either a normal matrix \mathbf{A}_\perp

$$\mathbf{A}_\perp = \begin{bmatrix} -1 & 0 \\ 0 & -2 \end{bmatrix} \quad (21)$$

or a non-normal matrix \mathbf{A}_\angle

$$\mathbf{A}_\angle = \begin{bmatrix} -1 & 5 \\ 0 & -2 \end{bmatrix}. \quad (22)$$

The spectral properties of these matrices are shown in Figs. 8(a)-8(b). The matrices have the same eigenvalues -1 s and -2 s and the same slowest-decaying eigenvectors \mathbf{e}_1 , which are parallel to the horizontal axis. However, while the other eigenvector of \mathbf{A}_\perp is along the vertical axis and hence orthogonal to \mathbf{e}_1 , the second eigenvector of \mathbf{A}_\angle is nearly anti-parallel to \mathbf{e}_1 with a 11.4° angle. As a result, \mathbf{A}_\angle is non-normal, i.e., $\mathbf{A}_\angle \mathbf{A}_\angle^\dagger \neq \mathbf{A}_\angle^\dagger \mathbf{A}_\angle$, and consequently, in spite of having negative eigenvalues, can lead to non-normal growth in \mathbf{z} and instability (see Fig. 1 in Trefethen (1991)). Non-normal operators are common in engineering and geophysical/astrophysical flows (see page 579 of Palmer (1999) for an illustrative example of why) and their significance for the dynamics of the atmosphere and ocean has been recognized through the pioneering papers of Farrell and his colleagues (e.g., Farrell 1988, 1989; Farrell and Moore 1992; Butler and Farrell 1992; Farrell and Ioannou 1996a,b) and those of others (e.g., Buizza and Palmer 1995; Penland and Sardeshmukh 1995; Ioannou 1995; Zanna and Tziperman 2005; Tziperman et al. 2008; Palmer and Zanna 2013).

For both matrices, Eq. (20) is integrated for $\mathbf{f} = 0$ using the Euler-Maruyama method with a 0.05 s timestep for 5 million seconds. The EOFs of the results are shown in Fig. 8(a)-8(b). For the normal matrix, EOF1 and EOF2 are almost identical to \mathbf{e}_1 and \mathbf{e}_2 , respectively, while they are different for the non-normal matrix. For both matrices, the results are used to construct $\hat{\mathbf{M}}_{\text{FDT}}$ from Eq. (18) without dimension-reduction (denoted as FDT-Full) and with only EOF1 retained (denoted as FDT-EOF1). The mean-responses of (20) with \mathbf{A}_\perp to external forcing $\mathbf{f} = \text{EOF1}$ predicted using FDT-Full and FDT-EOF1 are shown in Figs. 8(c). Both full and dimension-reduced LRF are very accurate. When the forcing has 10% projection onto EOF2, the LRF calculated using FDT-EOF1 shows a small error, because it cannot capture the part of the response that project onto EOF2 and is forced by the EOF2 component of \mathbf{f} . This becomes clear when (20) is transformed into the EOF-space:

$$\dot{\mathbf{a}} = [\mathbf{EOF}^{-1} (\mathbf{EIG} \mathbf{A} \mathbf{EIG}^{-1}) \mathbf{EOF}] \mathbf{a} + \mathbf{EOF}^{-1} \mathbf{f} \quad (23)$$

where $\mathbf{a} = (a_1, a_2)$ is a vector of the coefficients of the EOF1 and EOF2, \mathbf{EOF} and \mathbf{EIG} are 2×2 matrices whose columns are the EOFs and eigenvectors of \mathbf{A} , respectively,

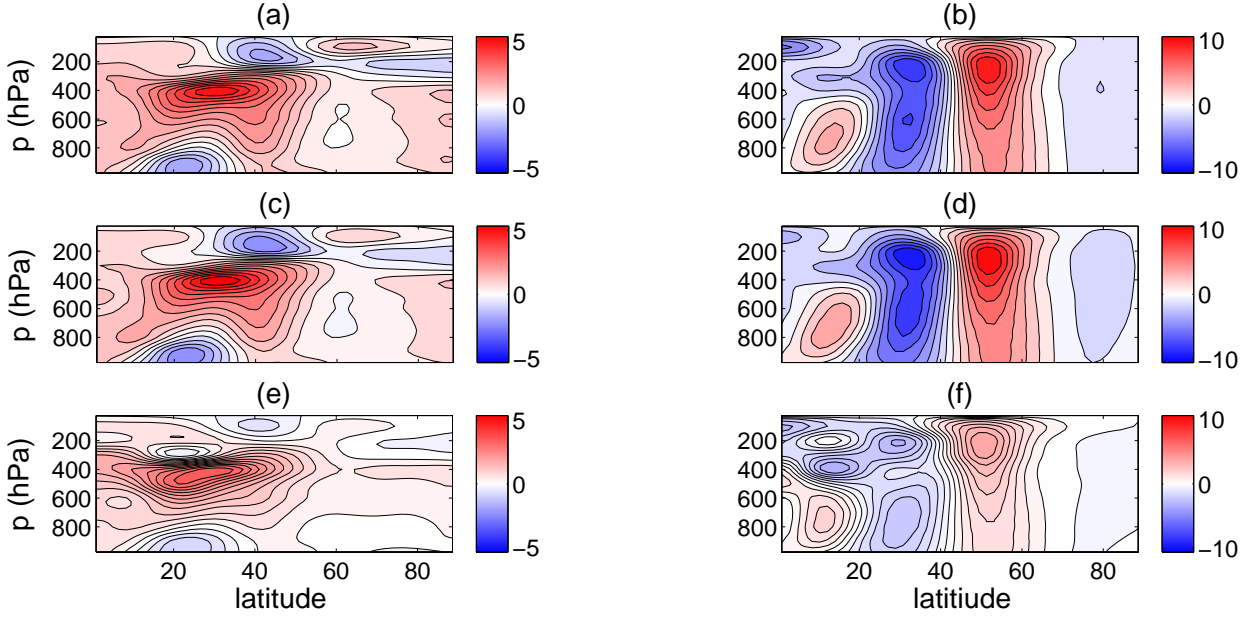


FIG. 7. Mean-response to a unit-amplitude thermal forcing of basis function centered at 30° and 400 hPa. Left (right) panels show temperature in K (zonal-wind in m s^{-1}). (a)-(b) the true response calculated using \mathbf{M} . (c)-(d) response calculated using \mathbf{M}_{FDT} without dimension reduction. Relative errors in amplitude are 11% (c) and 8% (d). (e)-(f) response calculated using \mathbf{M}_{FDT} with dimension reduction using the first 81 EOFs. Relative errors in amplitude are 31% and 62%. If only the component of the response that projects onto the first 81 EOFs is compared, the relative errors in amplitude are 12% (c), 8% (d), 25% (e), and 64% (f). Results of (c)-(f) are obtained with $\tau_\infty = 50$ days.

and $\mathbf{\Lambda}$ is a diagonal matrix of the eigenvalues of \mathbf{A} . The last term is simply a vector of the projections of \mathbf{f} onto the EOFs. The noise term is ignored for convenience. For a normal matrix such as \mathbf{A}_\perp , \mathbf{EOF} and \mathbf{EIG} are identical and the first term on the right-hand side reduces to $\mathbf{\Lambda} \mathbf{a}$. Hence the equations for a_1 and a_2 decouple. Then if \mathbf{f} does not have any projection on EOF2, $\langle a_2 \rangle = 0$ and FDT-EOF1 works as accurately as FDT-Full (Fig. 8(c)). If \mathbf{f} has a projection onto EOF2, then $\langle a_2 \rangle \neq 0$ causes some errors in FDT-EOF1, which can still accurately calculate $\langle a_1 \rangle$ (Fig. 8(e)).

However, for non-normal matrices $\mathbf{EOF} \neq \mathbf{EIG}$ (Fig. 8(b)) and the off-diagonal elements of the matrix in the first term on the right-hand side of (23) can be large, which strongly couple the two equations. In this case, a forcing that only projects onto EOF1 can result in large $\langle a_2 \rangle$, and part of a forcing that projects onto EOF2, even if small, can have a large contribution to $\langle a_1 \rangle$. Neither effects can be captured by FDT-EOF1 which can lead to large errors, as shown in Figs. 8(d) and 8(f) for \mathbf{A}_\perp . The amplitude of these errors depends on the non-normality of \mathbf{A} . For example, as shown in Fig. 9, for the same forcing \mathbf{f} which has a 10% contribution from EOF2, the error in the response predicted using FDT-EOF1 rapidly increases as the acute angle between the eigenvectors of \mathbf{A} decreases. The decrease in the angle results in a larger off-diagonal

term (coefficient of a_2) in the equation of a_1 , which explains the increase in the error.

The effect of non-normality complicates understanding the relationship between the error in dimension-reduced FDT predictions and the unresolved part of the forcings. For example, non-normality might explain why Fuchs et al. (2015) could not find a simple scaling relation between the error in the amplitude of the response and the loss of amplitude of the forcing due to dimension-reduction. While the error in prediction using FDT-EOF1 for a normal matrix is proportional to the percentage of the forcing that projects onto EOF2, the relationship is not linear for a non-normal matrix (see Fig. S5). Finally it should be noted that while here we have focused on the effect of non-normality on the errors in the mean-response arising from dimension-reduction, non-normality can also induce errors in the forcing calculated using dimension-reduced FDT for a given mean-response in a similar way.

The analyses presented in this section show that dimension-reduction alone can be a substantial source of error in the results obtained from LRFs constructed using FDT because of the non-normality of the system's operator, and demonstrate that the error depends on the relationship between the included and excluded EOFs, eigenvectors of the system's true operator, and the projections of the forcing/response onto the eigenvectors and EOFs. Based on these results, it is likely that errors arising from

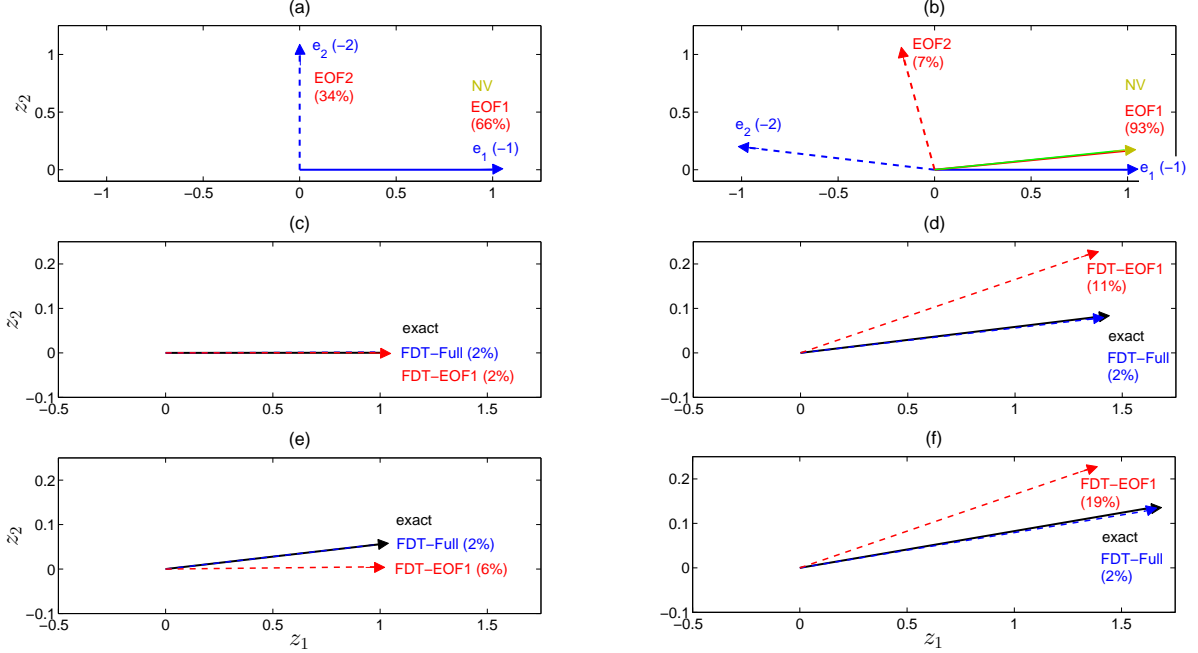


FIG. 8. Comparison of the performance of FDT in calculating the mean-response of Eq. (20) with normal matrix \mathbf{A}_\perp (left) and non-normal matrix \mathbf{A}_\parallel (right). (a)-(b): the blue arrows show the eigenvectors \mathbf{e}_1 and \mathbf{e}_2 with eigenvalues in parentheses; the red arrows show the EOFs with the explained variance in parentheses for $\mathbf{f} = 0$; and the green arrows show the neutral vectors (NV). In (a), \mathbf{e}_1 , EOF1, and NV are almost identical (as well as \mathbf{e}_2 and EOF2). In (b), EOF1 and NV are very close. The similarity between EOF1 and NV is expected following the discussion in section 5. (c)-(d): the end of the blue and red arrows show the mean-responses to unit-amplitude forcing $\mathbf{f} = \text{EOF1}$ obtained, respectively, from full FDT (FDT-Full) and dimension-reduced FDT that only uses EOF1 (FDT-EOF1). The black arrow shows the exact response and the parentheses show the relative error in $\|\cdot\|_2$. (e)-(f) same as (c)-(d) but for unit-amplitude forcing $\mathbf{f} = (0.9 \times \text{EOF1} + 0.1 \times \text{EOF2}) / \|0.9 \times \text{EOF1} + 0.1 \times \text{EOF2}\|_2$.

dimension-reduction are a major, if not the main, contributor to the poor performance of the LRF calculated using FDT in subsection 7.b. This is further supported by the fact that the best performance of FDT is achieved for Test 3 where the response projects mostly only onto EOF1 (there is little projection onto other EOFs due to the different weightings used in EOF calculations in sections 4 and 7.b).

It should be noted that the problem with non-normality and dimension-reduction discussed here cannot be resolved just by including more EOFs in the LRF construction, because the poorly sampled EOFs degrade the accuracy of LRF, and excluding them is the rationale behind the dimension-reduction strategy. In fact as reported by Fuchs et al. (2015) and also found here, including too many EOFs reduces the accuracy of $\hat{\mathbf{M}}_{\text{FDT}}$. Furthermore, only focusing on forcings/responses that strongly project onto the leading EOFs is an imperfect solution because it can seriously limit the applications of $\hat{\mathbf{M}}_{\text{FDT}}$, as many phenomena of interest do not project onto the natural modes of variability (see, e.g., Scaife et al. 2009).

The role of non-normality might explain the mixed success and difficulty in understanding some of the results obtained using FDT in other studies. Given that dimension-

reduction is inevitable for calculating LRFs using FDT from limited datasets and that non-normality is common in the oceanic and atmospheric flows, we suggest further investigations of dimension-reduction strategies with a focus on non-normality. Furthermore, we suggest that the linear stochastic equation (19) can be helpful in evaluating various strategies related to FDT and in disentangling the contributions of different sources of error because while this equation closely retains the complexity of a full GCM through $\hat{\mathbf{M}}$, it is computationally-inexpensive to solve and flexible in terms of the driving noise. For example, replacing ζ with correlated additive and multiplicative noise allows non-Gaussian statistics (Sardeshmukh and Sura 2009), which provides a simple framework to investigate the performance of FDT in non-Gaussian systems.

8. Summary

We have calculated the LRF ($\hat{\mathbf{M}}$) and EFM ($\hat{\mathbf{E}}$) for an idealized dry GCM using Green's functions and described the procedure in details (sections 2-3). Several tests in section 4 show that the LRF accurately predicts the mean-response to imposed thermal/mechanical forcings and vice versa and the EFM accurately predicts changes in eddy

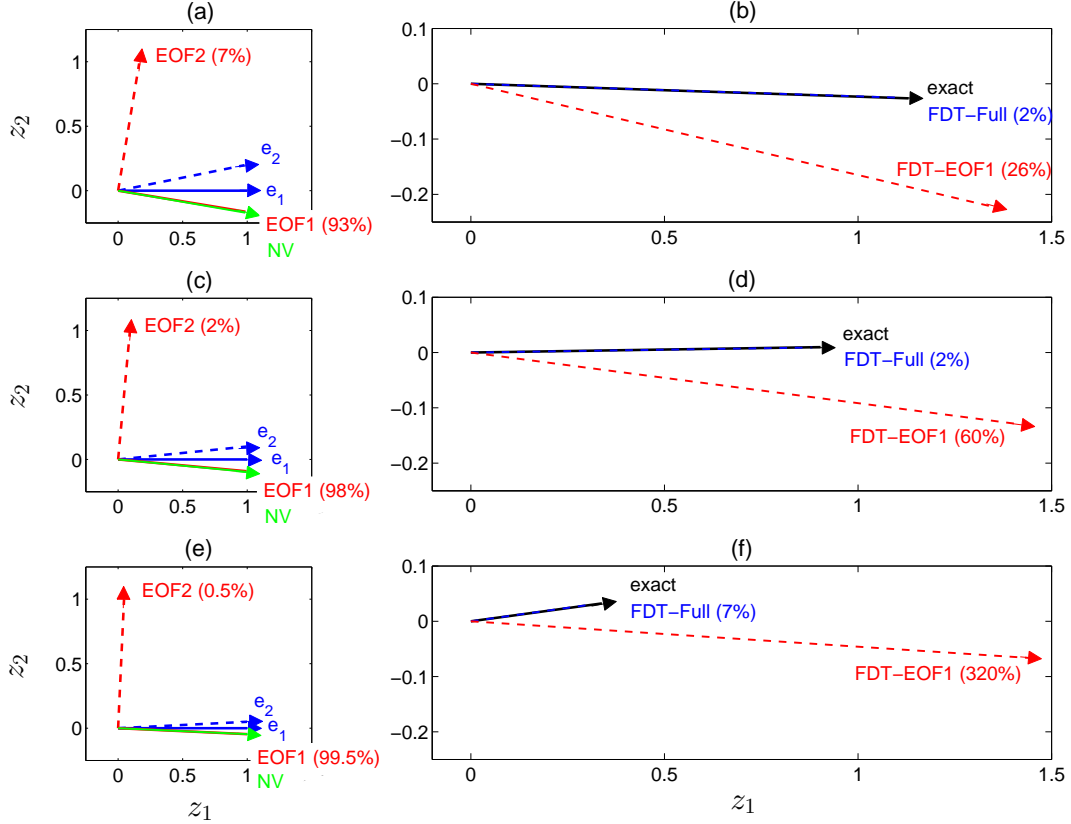


FIG. 9. Performance of the dimension-reduced FDT in calculating the mean-response of Eq. (20) to unit-amplitude forcing $\mathbf{f} = (0.9 \times \text{EOF1} + 0.1 \times \text{EOF2}) / \|(0.9 \times \text{EOF1} + 0.1 \times \text{EOF2})\|_2$ for three non-normal matrices with different angles between eigenvectors, which are, from top to bottom, $\sim 11.4^\circ$, 5.8° , and 2.8° . Left panels: the blue arrows show the eigenvectors \mathbf{e}_1 and \mathbf{e}_2 , which have eigenvalues -1 and -2 , respectively; the red arrows show the EOFs with the explained variance in parentheses for $\mathbf{f} = 0$; and the green arrows show the neutral vectors (NV). Right panels: for matrices on the left panels, the end of the blue and red arrows show the responses, respectively, from the full (FDT-Full) and dimension-reduced FDT that only uses EOF1 (FDT-EOF1). The black arrow shows the exact response and the parentheses show the relative error in $\|\cdot\|_2$.

fluxes in response to a change in the mean-flow. The spectral analysis of the LRF (section 5) reveals that the model's most excitable mode, i.e., the neutral vector, strongly resembles its Annular Mode, in particular for zonal-wind, which suggests that the Annular Mode is truly a dynamical mode of the system and explains the ubiquity of Annular Mode-like responses to external forcings. In section 6 we discuss the potential applications of $\hat{\mathbf{M}}$ and $\hat{\mathbf{E}}$ which include i) forcing a specified mean-flow for hypothesis-testing, ii) isolating and quantifying eddy-feedbacks in eddy-mean flow interaction problems, and iii) examining and evaluating more generally-applicable methods such as the FDT.

In section 7 we have also calculated the LRF from one million days of unforced simulation using multivariate fluctuation-dissipation theorem (FDT). We find $\hat{\mathbf{M}}_{\text{FDT}}$ to have qualitative skills in all the tests but quantitative skills only for some, consistent with the results of previous studies. To identify the source(s) of errors, we use long inte-

grations of linear stochastic equations whose operators are $\hat{\mathbf{M}}$ or 2×2 matrices and show that dimension-reduction through projecting the data onto the leading EOFs, which is needed to calculate the LRF from limited datasets using FDT, can alone cause significant errors due to the non-normality of the system's operator. These analyses suggest that future developments of practical strategies for FDT should consider non-normality and that examining non-normality can help with better interpreting and understanding the results obtained using FDT.

Acknowledgments. We thank Ashkan Borna, Nick Lutsko, and Saba Pasha for fruitful discussions; Marty Singh for useful comments on the manuscript; and Chris Walker for help with the GCM runs at the initial stage of this study. This work was supported by a Ziff Environmental Fellowship from the Harvard University Center for the Environment to P.H and NSF grant AGS-1062016 to Z.K. The simulations were run on Harvard Odyssey cluster.

APPENDIX A

We start from Eq. (5)

$$\dot{\bar{\mathbf{x}}} = \mathbf{L}\bar{\mathbf{x}} + \bar{\mathbf{f}} \quad (\text{A1})$$

which is the zonally-averaged primitive equations consisting of the three momentum equations, buoyancy equation, and continuity equation with $\bar{\mathbf{x}} = (\bar{u}, \bar{v}, \bar{\omega}, \bar{T}, \bar{\phi})$. $\bar{\mathbf{f}}$ is external forcing of zonal-momentum and/or buoyancy. Some of the operators or equations discussed below are derived/presented in details in Appendix A of Ring and Plumb (2008) and the reader is referred to the relevant equation number when possible; however, caution is required as the derivation in Ring and Plumb (2008) is for a state-vector that only consists of \bar{u} .

Using the continuity equation, \bar{v} and $\bar{\omega}$ can be represented using streamfunction χ (A3-A4 in Ring and Plumb (2008)) and the zonal-momentum and buoyancy equations of (A1) can be written as

$$\dot{\bar{\mathbf{y}}} = \hat{\mathbf{L}}\bar{\mathbf{y}} + \mathbf{H}\chi + \bar{\mathbf{f}} \quad (\text{A2})$$

where $\hat{\mathbf{L}}$ contains the relevant elements of \mathbf{L} . Operator \mathbf{H} is a function of $\langle \bar{U} \rangle$ and $\langle \bar{\Theta} \rangle$ and the second term on the right-hand side of (A2) represents meridional advection of these quantities by χ . Using the gradient-wind balance, which results from combining the meridional and vertical momentum equations, the tendency terms from the left-hand side of (A2) can be eliminated. This leads to a diagnostic equation for χ (similar to Eqs. A6-A7 and A10 in Ring and Plumb (2008))

$$\chi = \mathbf{G}\bar{\mathbf{y}} + \mathbf{K}\bar{\mathbf{f}}. \quad (\text{A3})$$

The first term on the right-hand side represents the component of χ due to $\bar{\mathbf{y}}$, and the second term represents the component of χ due to the part of $\bar{\mathbf{f}}$ that is not in gradient-wind balance (if any). The latter is related to the Eliassen's balanced vortex problem (Eliassen 1951) and Eq. A11 of Ring and Plumb (2008).

Substituting (A3) in (A2) and rearranging the terms yield

$$\dot{\bar{\mathbf{y}}} = (\hat{\mathbf{L}} + \mathbf{H}\mathbf{G})\bar{\mathbf{y}} + (\mathbf{I} + \mathbf{H}\mathbf{K})\bar{\mathbf{f}} \quad (\text{A4})$$

Equation 7 follows with defining $\mathbf{M} \equiv \hat{\mathbf{L}} + \mathbf{H}\mathbf{G}$ and $\mathbf{B} \equiv \mathbf{I} + \mathbf{H}\mathbf{K}$. \mathbf{B} only depends on $\langle \bar{U} \rangle$ and $\langle \bar{\Theta} \rangle$ and if needed, can be analytically calculated for the Held-Suarez setup as was done in Ring and Plumb (2008).

APPENDIX B

Choosing the appropriate forcing amplitude \bar{f}_o in each trial can be challenging, which is a common issue in problems involving LRFs. As note by Leith (1975) and Ring

and Plumb (2008), obtaining statistically robust results (i.e., large signal-to-noise ratios) and maintaining the linear regime (assumption 1) at the same time is difficult because the former requires strong forcings while the latter requires small forcings. What further complicates the problem for the current study (and likely for other studies involving the large-scale circulation) is that the response of the extratropics to external forcings projects strongly onto the leading pattern of internal variability (i.e., the Annular Modes), which makes it difficult to distinguish the signal from the noise. The projection of forced responses onto patterns of internal variability is seen in GCMs with various degree of complexity (e.g., Ring and Plumb 2007; Butler et al. 2010; Deser et al. 2004) and in observations (Corti et al. 1999; Thompson and Solomon 2002) and has been discussed in the context of FDT (e.g., Shepherd 2014) and neutral vectors (Palmer 1999; Goodman and Marshall 2002) (also see section 5).

We choose \bar{f}_o by trial-and-error, at least for the early trials, where we explore selected (μ_o, p_o) for $\mu_o = 0^\circ, 30^\circ, 60^\circ, 90^\circ$ and $p_o = 300, 600, 900$ hPa to find \bar{f}_o that produces a reasonable signal-to-noise ratio within the linear regime for each (μ_o, p_o) and each variable (U or Θ). Knowing acceptable \bar{f}_o of these selected trials, \bar{f}_o for other trials can be reasonably guessed (in some cases further trial-and-error is needed). To determine whether a forcing amplitude is acceptable, we employ three criteria (one qualitative and two quantitative) to evaluate the signal-to-noise ratio and linearity using the inter-hemispheric asymmetry of each trial and differences between the trials forced with $\pm \bar{f}_o$:

1. We visually inspect the hemispheric-symmetry in each of the following four patterns $\langle \bar{U} \rangle_{\pm}$ and $\langle \bar{\Theta} \rangle_{\pm}$. Large asymmetries indicate (qualitatively) small signal-to-noise ratios. We also visually compare the patterns of hemispherically-averaged $\langle \bar{U} \rangle_{+}$ with $\langle \bar{U} \rangle_{-}$, and $\langle \bar{\Theta} \rangle_{+}$ with $\langle \bar{\Theta} \rangle_{-}$. Large differences indicate small signal-to-noise ratios and/or nonlinearity, both of which are undesirable. We require these differences and asymmetries to be reasonably small.
2. Two measures of relative error e are calculated:

$$e(a) \equiv \frac{||a_{+} - a_c|| - ||a_{-} - a_c||}{(||a_{+} - a_c|| + ||a_{-} - a_c||)/2} \times 100 \quad (\text{B1})$$

where a is hemispherically-averaged $\langle \bar{U} \rangle$ or $\langle \bar{\Theta} \rangle$ and the norms are either

$$||a||_{\infty} \equiv \max(|a|) \quad (\text{B2})$$

$$||a||_2 \equiv \sqrt{\Sigma a^2} \quad (\text{B3})$$

where max and Σ are over the latitude-pressure domain. Large e_2 or e_{∞} show small signal-to-noise ratios and/or nonlinearity. We require e_2 and e_{∞} to be $\leq 20\%$ for both variables.

3. A measure of the signal-to-noise ratio is defined as

$$\text{SNR}(a_{\pm}) \equiv \frac{\|(a_{\pm} - a_c)_{\text{NH}} + (a_{\pm} - a_c)_{\text{SH}}\|_{\infty}}{\|(a_{\pm})_{\text{NH}} - (a_{\pm})_{\text{SH}}\|_{\infty}} \quad (\text{B4})$$

where NH (SH) refer to the Northern (Southern) hemisphere, and a is either $\langle \bar{U} \rangle$ or $\langle \bar{\Theta} \rangle$. We require SNR to be at least 3 for both variables although the number is larger than 5 in most accepted trials.

A forcing amplitude \tilde{f}_o is acceptable for each basis function and used in the calculation of $\tilde{\mathbf{M}}$ if all the three criteria are satisfied. The accepted values of \tilde{f}_o are shown in Tables S1-S2 (Supplemental Material). As a rule of thumb, stronger forcings are needed poleward and toward the surface, and for U compared to Θ . In Fig. B1 we show an example of the typical results from a pair of trials that are accepted and used in the calculation of the LRF and EFM.

Finally, it should be mentioned that external torque at the highest pressure level (~ 9 hPa) is found to result in unrealistically large responses in the tropical stratosphere. To avoid this problem, the basis functions of the zonal-wind for $p_o = 100$ hPa are set to zero at the highest pressure level and small-amplitude forcings are applied.

References

- Abramov, R. V., and A. J. Majda, 2007: Blended response algorithms for linear fluctuation-dissipation for complex nonlinear dynamical systems. *Nonlinearity*, **20** (12), 2793, doi:10.1088/0951-7715/20/12/004.
- Achatz, U., U. Löbl, S. I. Dolaptchiev, and A. Gritsun, 2013: Fluctuation–Dissipation supplemented by nonlinearity: A climate-dependent subgrid-scale parameterization in low-order climate models. *J. Atmos. Sci.*, **70** (6), 1833–1846, doi:10.1175/JAS-D-12-0229.1.
- Barnes, E. A., and J. A. Screen, 2015: The impact of Arctic warming on the midlatitude jet-stream: Can it? has it? will it? *WIREs Clim. Change*, **6** (3), 277–286, doi:10.1002/wcc.337.
- Bell, T. L., 1980: Climate sensitivity from fluctuation dissipation: Some simple model tests. *J. Atmos. Sci.*, **37** (8), 1700–1707, doi:10.1175/1520-0469(1980)037<1700:CSFFDS>2.0.CO;2.
- Berner, J., and G. Branstator, 2007: Linear and nonlinear signatures in the planetary wave dynamics of an AGCM: Probability density functions. *J. Atmos. Sci.*, **64** (1), 117–136, doi:10.1175/JAS3822.1.
- Berner, J., and Coauthors, 2015: Stochastic parameterization: towards a new view of weather and climate models. *arXiv:1510.08682v1*.
- Branstator, G., and S. E. Haupt, 1998: An empirical model of barotropic atmospheric dynamics and its response to tropical forcing. *J. Climate*, **11** (10), 2645–2667, doi:10.1175/1520-0442(1998)011<2645:AEMOBA>2.0.CO;2.
- Buizza, R., and T. N. Palmer, 1995: The singular-vector structure of the atmospheric global circulation. *J. Atmos. Sci.*, **52** (9), 1434–1456, doi:10.1175/1520-0469(1995)052<1434:TSVSOT>2.0.CO;2.
- Butler, A. H., D. W. J. Thompson, and R. Heikes, 2010: The steady-state atmospheric circulation response to climate change-like thermal forcings in a simple general circulation model. *J. Climate*, **23** (13), 3474–3496, doi:10.1175/2010JCLI3228.1.
- Butler, K. M., and B. F. Farrell, 1992: Three-dimensional optimal perturbations in viscous shear flow. *Phys. Fluids*, **4** (8), 1637–1650.
- Chen, G., and I. M. Held, 2007: Phase speed spectra and the recent poleward shift of Southern Hemisphere surface westerlies. *Geophys. Res. Lett.*, **34** (21), doi:10.1029/2007GL031200.
- Cionni, I., G. Visconti, and F. Sassi, 2004: Fluctuation dissipation theorem in a general circulation model. *Geophys. Res. Lett.*, **31** (9), doi:10.1029/2004GL019739.
- Cooper, F. C., J. G. Esler, and P. H. Haynes, 2013: Estimation of the local response to a forcing in a high dimensional system using the fluctuation-dissipation theorem. *Nonlin. Processes Geophys.*, **20** (2), 239–248, doi:10.5194/npg-20-239-2013.
- Corti, S., F. Molteni, and T. N. Palmer, 1999: Signature of recent climate change in frequencies of natural atmospheric circulation regimes. *Nature*, **398** (6730), 799–802, doi:10.1038/19745.
- DelSole, T., 2004: Stochastic models of quasigeostrophic turbulence. *Surv. Geophys.*, **25** (2), 107–149, doi:10.1023/B:GEOP.0000028160.75549.0d.
- Deser, C., G. Magnusdottir, R. Saravanan, and A. Phillips, 2004: The effects of North Atlantic SST and sea ice anomalies on the winter circulation in CCM3. Part II: Direct and indirect components of the response. *J. Climate*, **17** (5), 877–889, doi:10.1175/1520-0442(2004)017<0877:TEONAS>2.0.CO;2.
- Deser, C., R. A. Tomas, and L. Sun, 2015: The role of ocean–atmosphere coupling in the zonal-mean atmospheric response to arctic sea ice loss. *J. Climate*, **28** (6), 2168–2186, doi:10.1175/JCLI-D-14-00325.1.
- Domeisen, D. I. V., L. Sun, and G. Chen, 2013: The role of synoptic eddies in the tropospheric response to stratospheric variability. *Geophys. Res. Lett.*, **40** (18), 4933–4937, doi:10.1002/grl.50943.
- Edmon, H. J., B. J. Hoskins, and M. E. McIntyre, 1980: Eliassen–Palm cross sections for the troposphere. *J. Atmos. Sci.*, **37** (12), 2600–2616, doi:10.1175/1520-0469(1980)037<2600:EPCSFT>2.0.CO;2.
- Eliassen, A., 1951: Slow thermally or frictionally controlled meridional circulation in a circular vortex. *Astrophys. Norveg.*, **5**, 19–60.
- Farrell, B. F., 1988: Optimal excitation of neutral Rossby waves. *J. Atmos. Sci.*, **45** (2), 163–172, doi:10.1175/1520-0469(1988)045<0163:OEONRW>2.0.CO;2.
- Farrell, B. F., 1989: Optimal excitation of baroclinic waves. *J. Atmos. Sci.*, **46** (9), 1193–1206, doi:10.1175/1520-0469(1989)046<1193:OEOWB>2.0.CO;2.
- Farrell, B. F., and P. J. Ioannou, 1996a: Generalized stability theory. part I: Autonomous operators. *J. Atmos. Sci.*, **53** (14), 2025–2040, doi:10.1175/1520-0469(1996)053<2025:GSTPIA>2.0.CO;2.
- Farrell, B. F., and P. J. Ioannou, 1996b: Generalized stability theory. part II: Nonautonomous operators. *J. Atmos. Sci.*, **53** (14), 2041–2053, doi:10.1175/1520-0469(1996)053<2041:GSTPIN>2.0.CO;2.
- Farrell, B. F., and P. J. Ioannou, 2003: Structural stability of turbulent jets. *J. Atmos. Sci.*, **60** (17), 2101–2118, doi:10.1175/1520-0469(2003)060<2101:SSOTJ>2.0.CO;2.
- Farrell, B. F., and A. M. Moore, 1992: An adjoint method for obtaining the most rapidly growing perturbation to oceanic flows. *J. Phys. Oceanogr.*, **22** (4), 338–349, doi:10.1175/1520-0485(1992)022<0338:AAMFOT>2.0.CO;2.
- Feldstein, S., and S. Lee, 1998: Is the atmospheric zonal index driven by an eddy feedback? *J. Atmos. Sci.*, **55** (19), 3077–3086, doi:10.1175/1520-0469(1998)055<3077:ITAZID>2.0.CO;2.
- Franzke, C., A. J. Majda, and G. Branstator, 2007: The origin of nonlinear signatures of planetary wave dynamics: Mean phase space tendencies and contributions from non-Gaussianity. *J. Atmos. Sci.*, **64** (11), 3987–4003, doi:10.1175/2006JAS2221.1.
- Franzke, C. L. E., T. J. O’Kane, J. Berner, P. D. Williams, and V. Lucarini, 2015: Stochastic climate theory and modeling. *WIREs Clim. Change*, **6** (1), 63–78, doi:10.1002/wcc.318.

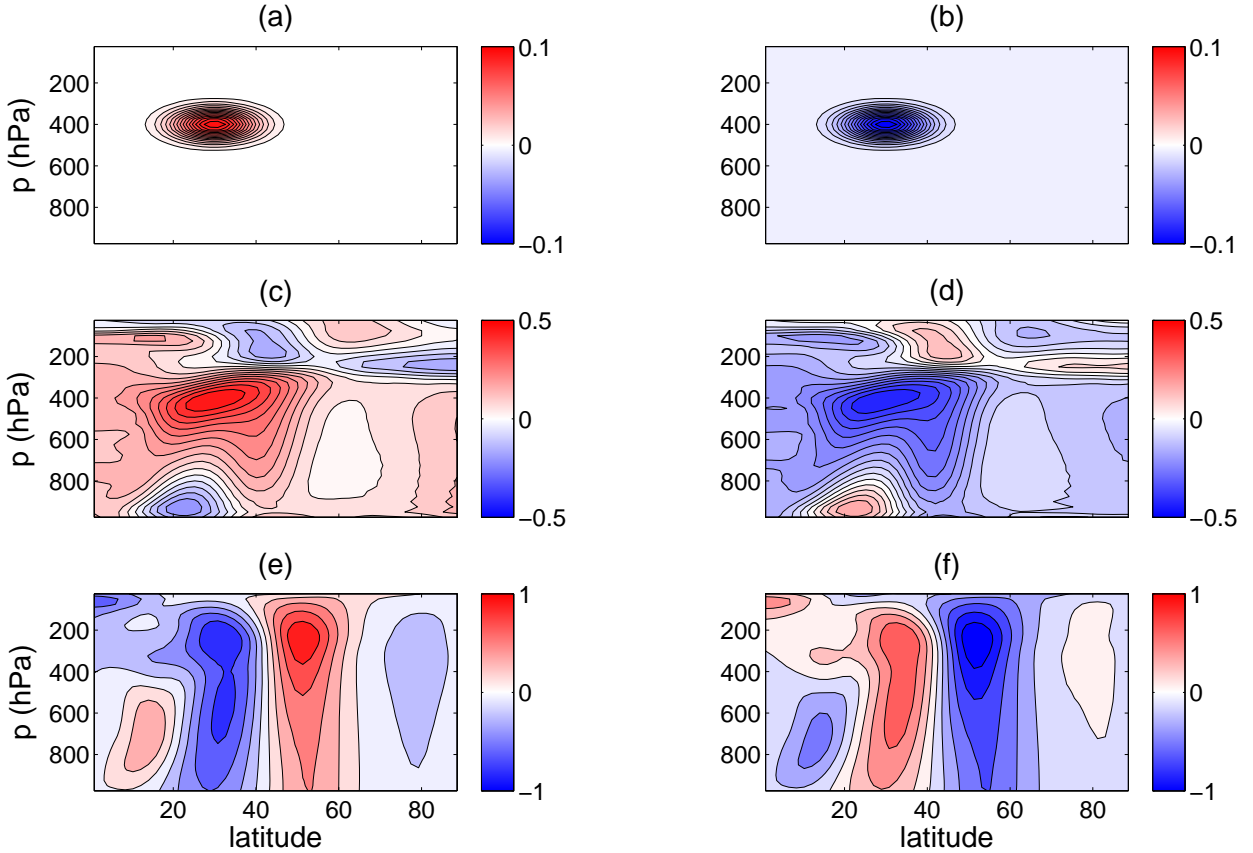


FIG. B1. Examples of results with imposed heating (left) and cooling (right) at $\mu_o = 30^\circ$ and $p_o = 400$ hPa with the amplitude of 0.1 K day^{-1} . Heating (a) and cooling (b) profiles. $\langle T \rangle = \langle \Theta \rangle_+ - \langle \Theta \rangle_c$ in K in response to heating (c) and cooling (d). $\langle \bar{u} \rangle = \langle \bar{U} \rangle_+ - \langle \bar{U} \rangle_c$ in m s^{-1} in response to heating (e) and cooling (f). The relative errors (e) and signal-to-noise ratios (SNR), defined in Eqs. (B1) and (B4), are $e_\infty(\langle \Theta \rangle) = 14\%$, $e_2(\langle \Theta \rangle) = 4\%$, $e_\infty(\langle \bar{U} \rangle) = 3\%$, $e_2(\langle \bar{U} \rangle) = 3\%$; $\text{SNR}(\langle T \rangle_+) = 17$ and $\text{SNR}(\langle T \rangle_-) = 5$; $\text{SNR}(\langle \bar{U} \rangle_+) = 12$ and $\text{SNR}(\langle \bar{U} \rangle_-) = 3$.

- Fuchs, D., S. Sherwood, and D. Hernandez, 2015: An exploration of multivariate fluctuation dissipation operators and their response to sea surface temperature perturbations. *J. Atmos. Sci.*, **72** (1), 472–486, doi:10.1175/JAS-D-14-0077.1.
- Garfinkel, C. I., D. W. Waugh, and E. P. Gerber, 2013: The effect of tropospheric jet latitude on coupling between the stratospheric polar vortex and the troposphere. *J. Climate*, **26** (6), 2077–2095, doi:10.1175/JCLI-D-12-00301.1.
- Gerber, E. P., L. M. Polvani, and D. Ancukiewicz, 2008a: Annular mode time scales in the intergovernmental panel on climate change fourth assessment report models. *Geophys. Res. Lett.*, **35** (22), doi:10.1029/2008GL035712.
- Gerber, E. P., S. Voronin, and L. M. Polvani, 2008b: Testing the annular mode autocorrelation time scale in simple atmospheric general circulation models. *Mon. Wea. Rev.*, **136** (4), 1523–1536, doi:10.1175/2007MWR2211.1.
- Gershgorin, B., and A. J. Majda, 2010: A test model for fluctuation-dissipation theorems with time-periodic statistics. *Physica D*, **239** (17), 1741–1757, doi:10.1016/j.physd.2010.05.009.
- Goodman, J. C., and J. Marshall, 2002: Using neutral singular vectors to study low-frequency atmospheric variability. *J. Atmos. Sci.*, **59** (22), 3206–3222, doi:10.1175/1520-0469(2002)059<3206:UNSVTS>2.0.CO;2.
- Gritsun, A., and G. Branstator, 2007: Climate response using a three-dimensional operator based on the fluctuation-dissipation theorem. *J. Atmos. Sci.*, **64** (7), 2558–2575, doi:10.1175/JAS3943.1.
- Gritsun, A., G. Branstator, and A. Majda, 2008: Climate response of linear and quadratic functionals using the fluctuation-dissipation theorem. *J. Atmos. Sci.*, **65** (9), 2824–2841, doi:10.1175/2007JAS2496.1.
- Hassanzadeh, P., and Z. Kuang, 2015: Blocking variability: Arctic Amplification versus Arctic Oscillation. *Geophys. Res. Lett.*, **42**, doi:10.1002/2015GL065923.
- Hassanzadeh, P., Z. Kuang, and B. F. Farrell, 2014: Responses of mid-latitude blocks and wave amplitude to changes in the meridional temperature gradient in an idealized dry GCM. *Geophys. Res. Lett.*, **41** (14), doi:10.1002/2014GL060764.
- Haynes, P. H., M. E. McIntyre, T. G. Shepherd, C. J. Marks, and K. P. Shine, 1991: On the downward control of extratropical diabatic circulations by eddy-induced mean zonal forces. *J. Atmos. Sci.*, **48** (4), 651–678, doi:10.1175/1520-0469(1991)048<0651:OTCOED>2.0.CO;2.
- Held, I. M., 2000: The general circulation of the atmosphere. *Proc. Prog. Geophys. Fluid Dyn.*, Woods Hole Oceanogr. Inst., <http://gfd.whoi.edu/proceedings/2000/PDFvol2000.html>.
- Held, I. M., and M. J. Suarez, 1994: A proposal for the intercomparison of the dynamical cores of atmospheric general circulation

- models. *Bull. Amer. Meteor. Soc.*, **75** (10), 1825–1830, doi:10.1175/1520-0477(1994)075<1825:APFTIO>2.0.CO;2.
- Herman, M. J., and Z. Kuang, 2013: Linear response functions of two convective parameterization schemes. *J. Adv. Model. Earth Syst.*, **5** (3), 510–541, doi:10.1002/jame.20037.
- Higham, D. J., 2001: An algorithmic introduction to numerical simulation of stochastic differential equations. *SIAM Rev.*, **43** (3), 525–546, doi:10.1137/S0036144500378302.
- Hoskins, B. J., and D. J. Karoly, 1981: The steady linear response of a spherical atmosphere to thermal and orographic forcing. *J. Atmos. Sci.*, **38** (6), 1179–1196, doi:10.1175/1520-0469(1981)038<1179:TSLROA>2.0.CO;2.
- Huybers, P., K. A. McKinnon, A. Rhines, and M. Tingley, 2014: US daily temperatures: The meaning of extremes in the context of nonnormality. *J. Climate*, **27** (19), 7368–7384, doi:10.1175/JCLI-D-14-00216.1.
- Ioannou, P. J., 1995: Nonnormality increases variance. *J. Atmos. Sci.*, **52** (8), 1155–1158, doi:10.1175/1520-0469(1995)052<1155:NIV>2.0.CO;2.
- Kidston, J., G. K. Vallis, S. M. Dean, and J. A. Renwick, 2011: Can the increase in the eddy length scale under global warming cause the poleward shift of the jet streams? *J. Climate*, **24**, 3764–3780, doi:10.1175/2010JCLI3738.1.
- Kraichnan, R. H., 1959: Classical fluctuation-relaxation theorem. *Phys. Rev.*, **113** (5), 1181, doi:10.1103/PhysRev.113.1181.
- Kuang, Z., 2004: The norm dependence of singular vectors. *J. Atmos. Sci.*, **61** (23), 2943–2949, doi:10.1175/JAS-3308.1.
- Kuang, Z., 2010: Linear response functions of a cumulus ensemble to temperature and moisture perturbations and implications for the dynamics of convectively coupled waves. *J. Atmos. Sci.*, **67** (4), 941–962, doi:10.1175/2009JAS3260.1.
- Kuang, Z., 2012: Weakly forced mock Walker cells. *J. Atmos. Sci.*, **69** (9), 2759–2786, doi:10.1175/JAS-D-11-0307.1.
- Kubo, R., 1966: The fluctuation-dissipation theorem. *Rep. Prog. Phys.*, **29** (1), 255–284, doi:10.1088/0034-4885/29/1/306.
- Kushner, P. J., and L. M. Polvani, 2004: Stratosphere-troposphere coupling in a relatively simple AGCM: The role of eddies. *J. Climate*, **17** (3), 629–639, doi:10.1175/1520-0442(2004)017<0629:SCIARS>2.0.CO;2.
- Lapeyre, G., and I. M. Held, 2003: Diffusivity, kinetic energy dissipation, and closure theories for the poleward eddy heat flux. *J. Atmos. Sci.*, **60** (23), 2907–2916, doi:10.1175/1520-0469(2003)060<2907:DKEDAC>2.0.CO;2.
- Leith, C. E., 1975: Climate response and fluctuation dissipation. *J. Atmos. Sci.*, **32** (10), 2022–2026, doi:10.1175/1520-0469(1975)032<2022:CRAFD>2.0.CO;2.
- Loikith, P. C., and J. D. Neelin, 2015: Short-tailed temperature distributions over north america and implications for future changes in extremes. *Geophys. Res. Lett.*, **42**, doi:10.1002/2015GL065602.
- Lorenz, D. J., 2014: Understanding midlatitude jet variability and change using Rossby wave chromatography: Poleward-shifted jets in response to external forcing. *J. Atmos. Sci.*, **71** (7), 2370–2389, doi:10.1175/JAS-D-13-0200.1.
- Lorenz, D. J., and D. L. Hartmann, 2001: Eddy-zonal flow feedback in the Southern Hemisphere. *J. Atmos. Sci.*, **58** (21), 3312–3327, doi:10.1175/1520-0469(2001)058<3312:EZFIFT>2.0.CO;2.
- Lutsko, N. J., I. M. Held, and P. Zurita-Gotor, 2015: Applying the fluctuation-dissipation theorem to a two-layer model of quasi-geostrophic turbulence. *J. Atmos. Sci.*, **72**, 3161–3177, doi:10.1175/JAS-D-14-0356.1.
- Majda, A. J., R. V. Abramov, and M. J. Grote, 2005: *Information theory and stochastics for multiscale nonlinear systems*, Vol. 25. American Mathematical Soc.
- Majda, A. J., B. Gershgorin, and Y. Yuan, 2010: Low-frequency climate response and fluctuation-dissipation theorems: theory and practice. *J. Atmos. Sci.*, **67** (4), 1186–1201, doi:10.1175/2009JAS3264.1.
- Marconi, U. M. B., A. Puglisi, L. Rondoni, and A. Vulpiani, 2008: Fluctuation–dissipation: response theory in statistical physics. *Phys. Rep.*, **461** (4), 111–195, doi:10.1016/j.physrep.2008.02.002.
- Marshall, J., and F. Molteni, 1993: Toward a dynamical understanding of planetary-scale flow regimes. *J. Atmos. Sci.*, **50** (12), 1792–1818, doi:10.1175/1520-0469(1993)050<1792:TADUOP>2.0.CO;2.
- Nakamura, N., and D. Zhu, 2010: Finite-amplitude wave activity and diffusive flux of potential vorticity in eddy-mean flow interaction. *J. Atmos. Sci.*, **67** (9), 2701–2716, doi:10.1175/2010JAS3432.1.
- Navarra, A., 1993: A new set of orthonormal modes for linearized meteorological problems. *J. Atmos. Sci.*, **50** (16), 2569–2583, doi:10.1175/1520-0469(1993)050<2569:ANSOOM>2.0.CO;2.
- Nie, J., and Z. Kuang, 2012: Responses of shallow cumulus convection to large-scale temperature and moisture perturbations: A comparison of large-eddy simulations and a convective parameterization based on stochastically entraining parcels. *J. Atmos. Sci.*, **69** (6), 1936–1956, doi:10.1175/JAS-D-11-0279.1.
- Nie, Y., Y. Zhang, G. Chen, X.-Q. Yang, and D. A. Burrows, 2014: Quantifying barotropic and baroclinic eddy feedbacks in the persistence of the Southern Annular Mode. *Geophys. Res. Lett.*, **41** (23), 8636–8644, doi:10.1002/2014GL062210.
- North, G. R., R. E. Bell, and J. W. Hardin, 1993: Fluctuation dissipation in a general circulation model. *Climate Dyn.*, **8** (6), 259–264, doi:10.1007/BF00209665.
- Nyquist, H., 1928: Thermal agitation of electric charge in conductors. *Phys. Rev.*, **32** (1), 110.
- Palmer, T. N., 1999: A nonlinear dynamical perspective on climate prediction. *J. Climate*, **12** (2), 575–591, doi:10.1175/1520-0442(1999)012<0575:ANDPOC>2.0.CO;2.
- Palmer, T. N., and L. Zanna, 2013: Singular vectors, predictability and ensemble forecasting for weather and climate. *J. Phys. A: Math. Theor.*, **46** (25), 254 018, doi:10.1088/1751-8113/46/25/254018.
- Pavan, V., and I. M. Held, 1996: The diffusive approximation for eddy fluxes in baroclinically unstable jets. *J. Atmos. Sci.*, **53** (9), 1262–1272, doi:10.1175/1520-0469(1996)053<1262:TDAFEF>2.0.CO;2.
- Peings, Y., and G. Magnusdottir, 2014: Response of the wintertime northern hemisphere atmospheric circulation to current and projected arctic sea ice decline: a numerical study with CAM5. *J. Climate*, **27** (1), 244–264, doi:10.1175/JCLI-D-13-00272.1.
- Penland, C., 1989: Random forcing and forecasting using principal oscillation pattern analysis. *Mon. Wea. Rev.*, **117** (10), 2165–2185, doi:10.1175/1520-0493(1989)117<2165:RFAFUP>2.0.CO;2.
- Penland, C., and P. D. Sardeshmukh, 1995: The optimal growth of tropical sea surface temperature anomalies. *J. Climate*, **8** (8), 1999–2024, doi:10.1175/1520-0442(1995)008<1999:TGOTS>2.0.CO;2.
- Reddy, S. C., P. J. Schmid, and D. S. Henningson, 1993: Pseudospectra of the Orr–Sommerfeld operator. *SIAM J. Appl. Math.*, **53** (1), 15–47, doi:10.1137/0153002.
- Ring, M. J., and R. A. Plumb, 2007: Forced annular mode patterns in a simple atmospheric general circulation model. *J. Atmos. Sci.*, **64** (10), 3611–3626, doi:10.1175/JAS4031.1.
- Ring, M. J., and R. A. Plumb, 2008: The response of a simplified GCM to axisymmetric forcings: Applicability of the fluctuation-dissipation theorem. *J. Atmos. Sci.*, **65** (12), 3880–3898, doi:10.1175/2008JAS2773.1.

- Riviere, G., 2011: A dynamical interpretation of the poleward shift of the jet streams in global warming scenarios. *J. Atmos. Sci.*, **68** (6), doi:10.1175/2011JAS3641.1.
- Robinson, W. A., 2000: A baroclinic mechanism for the eddy feedback on the zonal index. *J. Atmos. Sci.*, **57** (3), 415–422, doi:10.1175/1520-0469(2000)057<0415:ABMFTE>2.0.CO;2.
- Ruff, T. W., and J. D. Neelin, 2012: Long tails in regional surface temperature probability distributions with implications for extremes under global warming. *Geophys. Res. Lett.*, **39** (4), doi:10.1029/2011GL050610.
- Sardeshmukh, P. D., and P. Sura, 2009: Reconciling non-Gaussian climate statistics with linear dynamics. *J. Climate*, **22** (5), 1193–1207, doi:10.1175/2008JCLI2358.1.
- Scaife, A. A., C. Buontempo, M. Ringer, M. Sanderson, C. Gordon, and J. F. B. Mitchell, 2009: Toward seamless prediction: Calibration of climate change projections using seasonal forecasts. *Bull. Amer. Meteor. Soc.*, **90** (10), 1549–1551, doi:10.1175/2009BAMS2753.1.
- Schneider, T., 2006: The general circulation of the atmosphere. *Annu. Rev. Earth Planet. Sci.*, **34**, 655–688, doi:10.1146/annurev.earth.34.031405.125144.
- Shepherd, T. G., 2014: Atmospheric circulation as a source of uncertainty in climate change projections. *Nat. Geosci.*, **7**, 703–708, doi:10.1038/NGEO2253.
- Simpson, I. R., P. Hitchcock, T. G. Shepherd, and J. F. Scinocca, 2013a: Southern annular mode dynamics in observations and models. part I: The influence of climatological zonal wind biases in a comprehensive GCM. *J. Climate*, **26** (11), 3953–3967, doi:10.1175/JCLI-D-12-00348.1.
- Simpson, I. R., T. G. Shepherd, P. Hitchcock, and J. F. Scinocca, 2013b: Southern annular mode dynamics in observations and models. part II: Eddy feedbacks. *J. Climate*, **26** (14), 5220–5241, doi:10.1175/JCLI-D-12-00495.1.
- Song, Y., and W. A. Robinson, 2004: Dynamical mechanisms for stratospheric influences on the troposphere. *J. Atmos. Sci.*, **61** (14), 1711–1725, doi:10.1175/1520-0469(2004)061<1711:DMFSIO>2.0.CO;2.
- Thompson, D. W. J., and Y. Li, 2015: Baroclinic and barotropic annular variability in the Northern Hemisphere. *J. Atmos. Sci.*, **72** (3), 1117–1136, doi:10.1175/JAS-D-14-0104.1.
- Thompson, D. W. J., and S. Solomon, 2002: Interpretation of recent Southern Hemisphere climate change. *Science*, **296** (5569), 895–899, doi:10.1126/science.1069270.
- Thompson, D. W. J., and J. D. Woodworth, 2014: Barotropic and baroclinic annular variability in the Southern Hemisphere. *J. Atmos. Sci.*, **71** (4), 1480–1493, doi:10.1175/JAS-D-13-0185.1.
- Trefethen, L. N., 1991: Pseudospectra of matrices. *Numerical analysis*, D. F. Griffiths, and G. A. Watson, Eds., Longman, 234–265.
- Trefethen, L. N., A. E. Trefethen, S. Reddy, T. Driscoll, and Coauthors, 1993: Hydrodynamic stability without eigenvalues. *Science*, **261** (5121), 578–584, doi:10.1175/JAS-3308.1.
- Tziperman, E., L. Zanna, and C. Penland, 2008: Nonnormal thermohaline circulation dynamics in a coupled ocean-atmosphere GCM. *J. Phys. Oceanogr.*, **38** (3), 588–604.
- Vallis, G. K., 2006: *Atmospheric and oceanic fluid dynamics: fundamentals and large-scale circulation*. Cambridge University Press.
- Zanna, L., and E. Tziperman, 2005: Nonnormal amplification of the thermohaline circulation. *J. Phys. Oceanogr.*, **35** (9), 1593–1605, doi:10.1175/JPO2777.1.
- Zhang, Y., and I. M. Held, 1999: A linear stochastic model of a GCM's midlatitude storm tracks. *J. Atmos. Sci.*, **56** (19), 3416–3435, doi:10.1175/1520-0469(1999)056<3416:ALSMOA>2.0.CO;2.